

Contents lists available at ScienceDirect

Mechanical Systems and Signal Processing

journal homepage: www.elsevier.com/locate/ymssp





Metaheuristic inverse analysis on interfacial mechanics of distributed fiber optic sensors undergoing interfacial debonding

Xiao Tan^a, Soroush Mahjoubi^a, Xingxing Zou^b, Weina Meng^a, Yi Bao^{a,*}

^a Department of Civil, Environmental and Ocean Engineering, Stevens Institute of Technology, Hoboken, NJ 07030, United States

ARTICLE INFO

Communicated by: Lukasz Jankowski

Keywords:
Crack assessment
Distributed fiber optic sensors
Interface mechanics
Metaheuristic inverse analysis
Optical frequency domain reflectometry
(OFDR)
Structural health monitoring

ABSTRACT

Distributed fiber optic sensors with protective packages have shown unique capabilities in measuring strain and crack distributions for structural health monitoring. However, the mechanics at the fiber-package interface remain unclear when debonding occurs. This paper investigates the interfacial mechanics for distributed fiber optic sensors undergoing debonding through mechanical analysis and metaheuristic-based inverse analysis. First, the governing equation of the interfacial mechanics is established and solved with assistance from metaheuristic-based inverse analysis on the interfacial properties of fiber optic cables. Then, experiments were conducted to validate the analysis results by measuring the strain distribution in distributed fiber optic sensors based on optical frequency domain reflectometry. The results showed that the proposed approach accurately quantified the interfacial mechanics, interfacial properties, strain transfer, and debonding behavior in distributed fiber optic sensors. This research advances the fundamental understandings of the sensing mechanisms of distributed fiber optic sensors undergoing inelastic behaviors for structural health monitoring.

1. Introduction

The conditions of structures during construction and operation concern public welfare and safety. The collapse of bridges and leaking of pipes can cause catastrophic consequences and capital loss. Structural health monitoring plays important roles in restoring structures through identifying, locating, and quantifying anomalies at early stages [1], enabling timely and efficient actions with high efficacy and low cost. Various sensor technologies have been developed to monitor structural conditions. Fiber optic sensors are attracting increasing interests due to their unique characteristics, such as high sensitivity, high accuracy, light weight, small size, physical and chemical stability, immunity to electromagnetic interference, and multiplexability [2,3].

According to the spatial features, fiber optic sensors are categorized into point sensors and distributed sensors [4]. A point sensor only provides measurements over its gauge length. Although it is possible to connect multiple point sensors to form a "quasi-distributed" sensor for measuring multiple discrete spots, the cost associated with sensor preparation and operation is increased in practice [2,3]. Alternatively, a distributed sensor has a unique advantage of utilizing a single fused silica optical fiber as both the transmission line and the sensor with dense sensing points, thus providing spatially distributed measurements. It is promising for automated condition monitoring and assessment of large-scale engineering structures [5]. With these attractive features, distributed fiber optic sensors are used to measure strain distributions in various engineering structures [1–5].

E-mail address: yi.bao@stevens.edu (Y. Bao).

^b College of Civil Engineering, Nanjing Forestry University, Nanjing, Jiangsu, China

^{*} Corresponding author.

An optical fiber is usually composed of a sensing fiber and coatings used to protect the fiber from damage under mechanical loads or various environmental effects [6,7]. The presence of the protective coatings influences the measurement from the sensor because the coating deformation changes the deformation sensed by the sensing fiber [8,9], known as the "strain transfer effect" in the context of fiber optic sensors [10]. Currently, fiber optic sensors are mainly operated under conditions with an intact fiber-coating interface [8–10]. The strain transfer effect is quantitatively considered by calibrating the strain transfer coefficients for point fiber optic sensors or analyzing the strain transfer equations for distributed fiber optic sensors [11–13].

Recent research found that fiber optic sensors were also applicable in the presence of fiber-coating interface debonding [11,14], and the interface debonding showed benefits for fiber optic sensors [10]. Fig. 1 shows a fiber optic cable embedded in a matrix subject to tensile forces. When the host matrix (e.g., steel or concrete) is cracked, the fiber-coating interface will be disturbed, and an interfacial slip will occur, thus altering the axial stresses in the fiber. Basically, the abrupt local deformation caused by the crack is redistributed over a longer length along the fiber. Such strain redistribution helps accommodate the localized deformation at the crack opening, thus reducing the peak tensile stress in the fiber and protecting the fiber from rupture [2]. The fiber-coating interface debonding helps avoid the rupture of distributed sensors crossing cracks [11,12]. Debonding is essential for using distributed fiber optic sensors in structural health monitoring because the occurrence of discontinuity such as cracks [11,12] and delamination/debonding [15] in host structures is unavoidable in practice.

Currently, there is lack of knowledge on the fiber-coating interfacial behavior [16]. Previous research on the interfacial strain transfer of fiber optic sensors focused on the elastic stage, lacking consideration of interfacial debonding. The strain transfer of a fused silica fiber with polymeric coating was studied in references [8–10,16]. It was assumed that the fused silica fiber was exposed to constant shear stress at the fiber-coating interface when debonding occurred [16]. However, the derived strain distributions in fused silica fibers were inconsistent with the strain distributions measured from high-resolution distributed sensors [11]. Multiple challenges have been identified from previous research: (1) The fiber-coating interfacial behavior is unclear, hindering accurate interpretation of sensor data. (2) It is difficult to determine the interfacial properties of sensors. Existing research on the interface laws relies on trial-and-error methods with limited efficiency and accuracy. The parameters were manually selected in references [17,18]. When there are many parameters, it will be challenging to obtain parameters using trial-and-error methods. In a nutshell, the interfacial bond-slip behavior of optical fibers is still unclear. When a distributed sensor is used to measure strains, the following questions need to be answered: (1) When will debonding be initiated between the fiber and coating? (2) How will the debonding propagate at the interface? (3) How will the debonding affect the strain distribution in fused silica fiber under the strain transfer effect? These knowledge gaps have stalled wider applications of distributed sensors because it is unknown how to properly interpret the distributed strain sensing data in the presence of cracks.

Motivated by these challenges, this research has three main objectives: (1) to develop a unified cohesive interface law (CIL) and a mechanical model to describe the interfacial behaviors; (2) to understand the fiber-coating interfacial behavior for distributed fiber optic sensors; and (3) to utilize distributed fiber optic sensors to measure the strain distributions in fused silica fibers in the presence of interfacial debonding. To this end, this research performed a mechanical analysis on the fiber-coating interface based on the CIL and intrinsically linked the CIL to the force-slip results in the fiber pullout process. The link was then used to calibrate the parameters of the CIL perform through a metaheuristic inverse analysis. Strain distributions in the fused silica fiber were directly measured using a fully distributed fiber optic sensing technology.

The novelties of this research include three aspects: (1) This research proposes a unified CIL to describe the fiber—matrix interface and derives closed-form solutions. (2) This research presents a metaheuristic inverse analysis approach to enabling the automatic determination of interfacial parameters. (3) The proposed CIL and analytical solutions are validated by measurements from distributed sensors. A unique feature of this research is that the research on interface mechanics and distributed sensing is integrated via a metaheuristic inverse analysis. This research advances the fundamental understanding on the interfacial behavior of distributed sensors and promotes the crack sensing capabilities. The clarification of interfacial behaviors will pave the theoretical way to understanding the sensor data and enable the use of distributed sensors in scenarios involving interface debonding, thus promoting the applications of distributed sensors in measuring cracks.

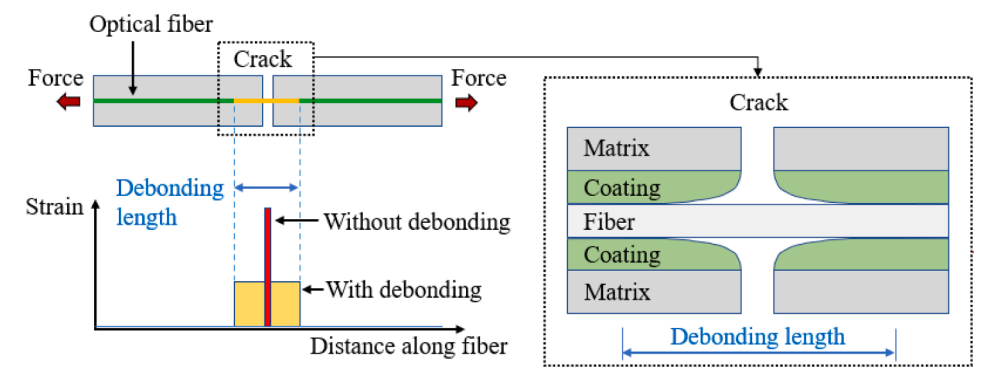


Fig. 1. Utilization of debonding at fiber-coating interface to avoid or delay fiber rupture in a distributed fiber optic sensor crossing a crack.

2. Methods

2.1. Framework

Fig. 2 shows the research framework. The black arrows show the flow of solving the problems in previous research, and the interface law is the key to addressing the challenges. The interface law is evaluated through the fiber pullout response, and the relation is established via a forward mechanical analysis. This research presents a unified CIL and proposes to determine the interface law using the fiber pullout test through the metaheuristic inverse analysis.

With the interface law, on one hand, the law is used to interpret the bond-slip behavior of the fiber-coating interface for fiber optic sensors, thus enabling distributed fiber optic sensors to measure cracks in presence of interfacial debonding. The interface law is used to predict the strain distributions in fused silica fiber during the fiber pullout process, and the prediction results are evaluated by using a distributed fiber optic sensor. On the other hand, the proposed CIL are independent of the specific materials and applicable to different types of composites to predict the mechanical properties of unknown fiber-reinforced interface, as marked by the green arrows. This research mainly focuses on the mechanical analysis based on the interface law, metaheuristic inverse analysis, and distributed sensing, as elaborated in Sections 2.2 to 2.4.

2.2. Mechanical analysis

2.2.1. Optical fiber

Fig. 3(a) shows the structure of a representative optical fiber (Corning, SMF-28e +) packaged with two layers of polymeric coating. The fiber has an 8.2-μm-diameter fused silica core, a 125-μm fused silica cladding, a 190-μm inner coating, and a 242-μm outer coating. Thereafter, the fused silica core and cladding are referred to as fiber core, and the inner and outer coatings are referred to as coating (see Fig. 3(b)). The sensing part is the fiber core. Light waves propagate along the fiber optic cable through total internal reflection at the core-cladding interface. The inner coating is soft and rubbery which cushions the fused silica fiber from external mechanical loads. Another important function of the inner coating is to facilitate operations such as stripping off the coatings without damaging the fused silica fiber. The inner coating is surrounded by the stiff outer coating that protects the fiber and inner coating from abrasions and environmental exposure.

In the manufacturing of optical fibers, the inner and outer coatings are applied sequentially in a liquid form as the glass fiber is drawn and are sequentially cured by exposure to ultraviolet light sources. Table 1 presents the dimensions and the elastic moduli of the different components of the optical fiber. There are three interfaces, which are the interfaces between: (i) fused silica fiber core and cladding, (ii) fused silica fiber cladding and primary (inner) coating, and (iii) primary coating and secondary (outer) coating. There are covalent bonds at the interfaces (i) and (iii) [19]. However, interface (ii) is mainly bonded via Van der Waals force [20]. Based on energy, the covalent bonds are stronger than Van der Waals force, so debonding occurs at interface (ii) under pulling forces.

2.2.2. Governing equation

Fig. 4 shows an infinitesimal segment of a fiber embedded in a matrix. The representative types of matrices for structures include the cementitious matrix such as mortar and the polymetric matrix such as epoxy resin. The optical fiber is composed of a fused silica fiber core and polymeric coating. The coating of the optical fiber is in direct contact with the matrix.

When the matrix is fixed, the fused silica fiber is subject to a pullout force P. The length of the optical fiber embedded in the matrix is \mathscr{E} , and the diameter of the fused silica fiber core is D_f . The axial stress in the fiber core is $\sigma_f(x)$, where x is the coordinate along the fiber length. The interfacial slip between fiber core and coating is s. The elastic modulus and section area of the representative types of host matrix for engineering structures are often much larger than those of the optical fiber. Therefore, the matrix deformation is neglected. Since the interfacial slip varies along the fiber length, s is written as s(x). The slip distances at the free end and the loaded end of the matrix are respectively denoted as $s_F = s(x = 0)$ and $s_G = s(x = \mathscr{E})$. The shear stress at the fiber-coating interface is a function of s and expressed as $\tau(s)$.

The equilibrium equation of the fused silica fiber along \times direction is expressed as:

$$\sigma_f(x) \bullet A_f + \tau(s)dx \bullet p_f = \left[\sigma_f(x) + d\sigma_f(x)\right] \bullet A_f \tag{1a}$$

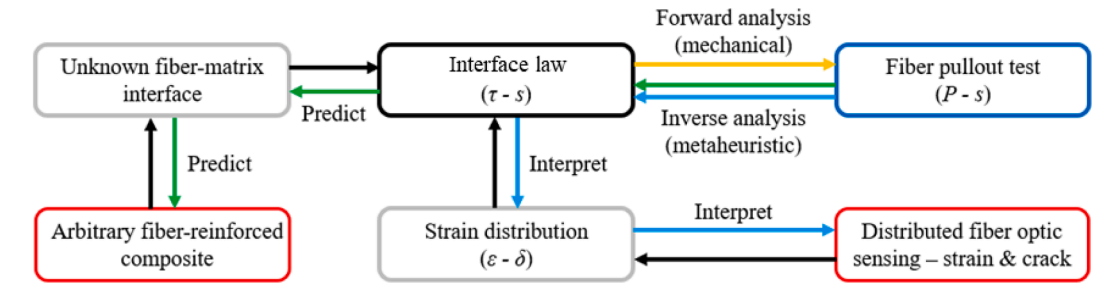


Fig. 2. Research framework integrating forward analysis, inverse analysis, and distributed fiber optic sensing of strains and cracks.

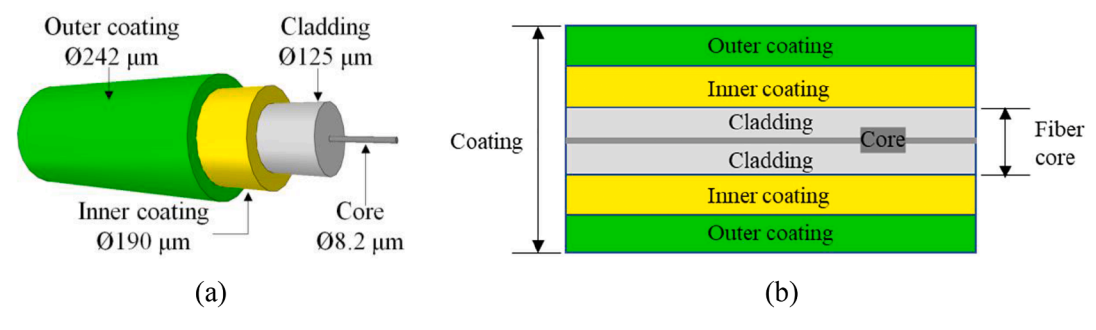


Fig. 3. Structure of single mode optical fibers with dual-layer polymeric coating: (a) components of a single mode optical fiber; and (b) typical layers of an optical fiber.

Table 1Main properties of the optical fiber.

Components		Material	Outer diameter	Elastic modulus	
Fiber core	Core	Fused silica	8.2 μm	70.2 GPa	
Coating	Cladding Inner coating Outer coating	Fused silica Acrylate Acrylate	125 μm 190 μm 242 μm	70.2 GPa 0.6 MPa 2550 MPa	

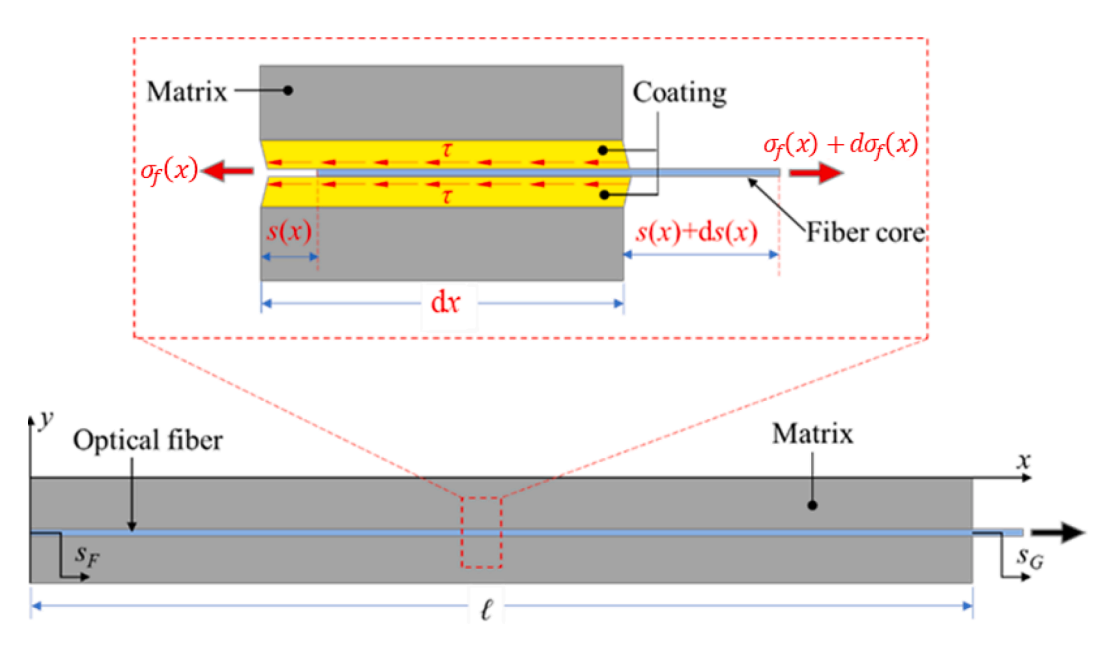


Fig. 4. Infinitesimal segment of an optical fiber embedded in a matrix and subject to a pulling force.

$$\sigma_c(x) \bullet A_c = \tau(s) dx \bullet p_f + [\sigma_c(x) + d\sigma_c(x)] \bullet A_c$$
(1b)

where $\sigma_c(x)$ and A_c are the axial stress in the coating and the cross-sectional area of coating, respectively; A_f and p_f are the cross-sectional area and perimeter of fiber core, respectively, which are expressed as:

$$A_f = \frac{1}{4}\pi D_f^2 \tag{2a}$$

$$p_f = \pi D_f \tag{2b}$$

Eq. (1) is rewritten as:

$$\frac{d\sigma_f(x)}{dx} = \frac{p_f}{A_f}\tau(s) \tag{3a}$$

$$\frac{d\sigma_c(x)}{dx} = -\frac{p_f}{A}\tau(s) \tag{3b}$$

According to the Hooke's Law, the relationship between the normal stress and strain along the fiber length is expressed in Eq. (4):

$$\sigma_f(x) = E_f \varepsilon_f(x) = E_f \frac{du_f(x)}{dx}$$
 (4a)

$$\sigma_c(x) = E_c \varepsilon_c(x) = E_c \frac{du_c(x)}{dx}$$
 (4b)

$$s(x) = u_r(x) - u_r(x) \tag{4c}$$

$$E_c = \frac{E_{ci}A_{ci} + E_{co}A_{co}}{A_{ci} + A_{co}} \tag{4d}$$

where E_f , E_{ci} , and E_{co} are the elastic moduli of the fiber core, inner coating, and outer coating, respectively; $u_f(x)$ and $u_c(x)$ are the displacement of fiber core and coating layers, respectively; A_{ci} and A_{co} are the cross-sectional areas of the inner and outer coatings, respectively.

Substituting Eq. (4) into Eq. (3) and Eq. (1), the governing equation is obtained:

$$\frac{d^2s(x)}{dx^2} - \lambda^2 \tau(s) = 0 \tag{5a}$$

$$\frac{ds(x)}{dx} = \varphi \varepsilon_f(x) \tag{5b}$$

$$w_c = 2[u_f(\ell) - u_f(0)] = \frac{2}{\varphi}(s_G - s_F) = 2\int_0^{\infty} \varepsilon_f(x)dx$$
 (5c)

where $\lambda = \sqrt{\frac{p_f \bullet \varphi}{E_f A_f}}$; $\varphi = \left(\frac{A_f E_f}{A_c E_c} + 1\right)$; w_c refers to the crack width.

The boundary conditions at the free end are:

$$\varepsilon_f(x=0)=0$$
 (6a)

$$s(x=0) = s_F \tag{6b}$$

The axial stress in the fiber core at the loaded end is expressed as:

$$\varepsilon_f(x=\ell) = \frac{P}{A_c E_c} \tag{7}$$

Eqs. (5a) and (5b) describe the relationship between the interfacial slip and shear stress [19]. Eq. (5c) provides a theoretical foundation for quantifying crack widths using the interfacial slip or integration of the strain distribution in vicinity of the crack. The interfacial bond-slip law is needed to solve the governing equation of the interface law, as elaborated in Section 2.2.3.

2.2.3. Unified CIL

This subsection presents a CIL to unify the bond-slip models of shear-softening and shear-hardening interfaces, as shown in Fig. 5. The CIL has three main stages: (i) a linear-elastic stage, (ii) a yielding stage, and (iii) a debonding stage. In the linear-elastic stage, as the slip increases from 0 to αs_f (0 < α < 1), the shear stress linearly increases from 0 to $\beta \tau_f$. In the yielding stage, as the slip increases from αs_f to s_f , the shear stress linearly changes from $\beta \tau_f$ to τ_f . If β > 1, the CIL describes a linear softening behavior, meaning that the interfacial shear stress deceases in the yielding stage. If β = 1, the CIL describes a constant behavior. If 0 < β < 1, the CIL describes a linear hardening behavior, meaning that the interfacial shear stress increases in the yielding stage. Finally, after the slip is larger than s_f , the debonding stage occurs, and the shear stress decreases with the interface slip exponentially.

The CIL is expressed as

$$\tau(s) = \begin{cases} \frac{\beta \tau_f}{\alpha s_f} s, 0 \le s \le \alpha s_f \\ \frac{\tau_f}{1 - \alpha} \left[\frac{(1 - \beta)s}{s_f} + (\beta - \alpha) \right], \alpha s_f < s \le s_f \\ \tau_f e^{\frac{-\tau_f \left(s - s_f\right)}{k}}, s_f \le s \end{cases}$$

$$(8)$$

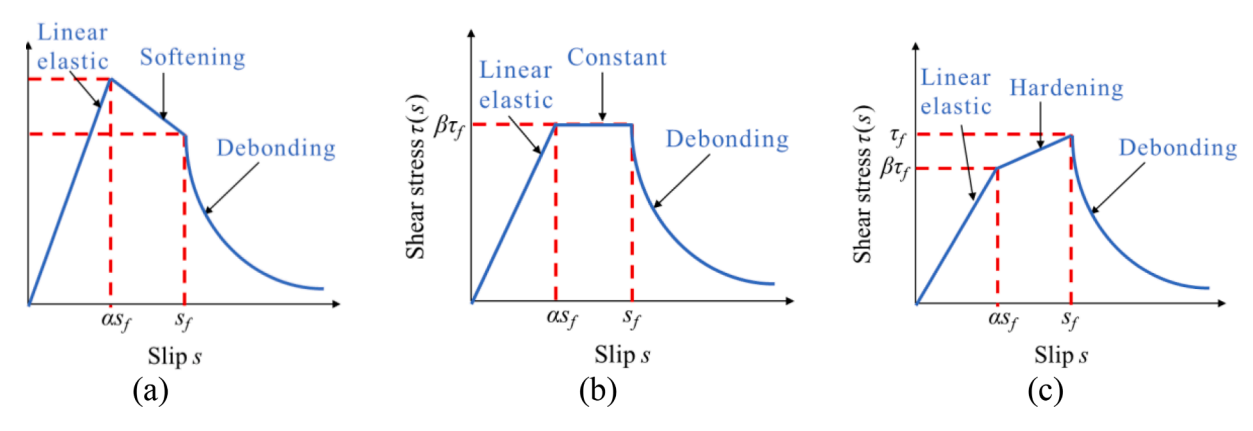


Fig. 5. Illustration of CIL: (a) softening interface ($\beta > 1$); (b) constant interface ($\beta = 1$); and (c) hardening interface ($0 < \beta < 1$).

where τ_f , s_f , α , β , and k are the unknown parameters of the CIL to be calibrated; τ_f (0 < $\beta \le 1$) or $\beta \tau_f$ ($\beta > 1$) refer to bond strength; s_f and k are the slip corresponding to the bond strength and interfacial fracture energy, respectively; α and β determine the separating point in the linear elastic ascending part of the CIL; and β is of crucial importance in the CIL because β determines the type of the interface. With Eq. (8), Eq. (5) can be solved, as elaborated in Section 3.

The main reason for adopting an exponential function in the debonding stage is that the exponential function can cover various cases, as shown in Fig. 6. When k approaches to 0 (e.g., k = 0.01), the exponential function tends to describe a null interfacial stress transfer (complete loss of adhesion) behavior. When k is between 3 and 100, the debonding stage shows a softening behavior. When k is larger than 100 (e.g., k = 400), the debonding stage tends to describe a constant residual stress behavior.

An advantage of the presented approach is that there is no need for assuming the debonding stage in advance. The proposed cohesive law can be applied to various cases, and the model parameters can be determined through the proposed inverse analysis approach. This is particularly important for many applications when the interfacial properties are unknown. This is the case for our research because there is little research on fiber–matrix interfacial properties of optical fibers.

2.3. Metaheuristic inverse analysis

This section presents the metaheuristic inverse analysis method to accurately calibrate the parameters of the CIL, as illustrated in Fig. 7. Past research showed that the force-slip curves of pullout tests were determined when a CIL was given through a forward analysis [17,18,21–32]. However, the calibration of the model parameters is an inverse problem, which was usually solved through the trial-and-error method. Nevertheless, the trial-and-error method is inefficient and inaccurate, especially when there are multiple parameters that involve coupling effects. Inaccurate model parameters highly affect the analysis accuracy of interfacial behaviors.

This study proposes to solve the inverse problem using the hypotrochoid spiral algorithm [33,34]. A set of initial values are assigned to the model parameters. With the initial values, the analytical solutions of force-slip data are calculated based on the forward

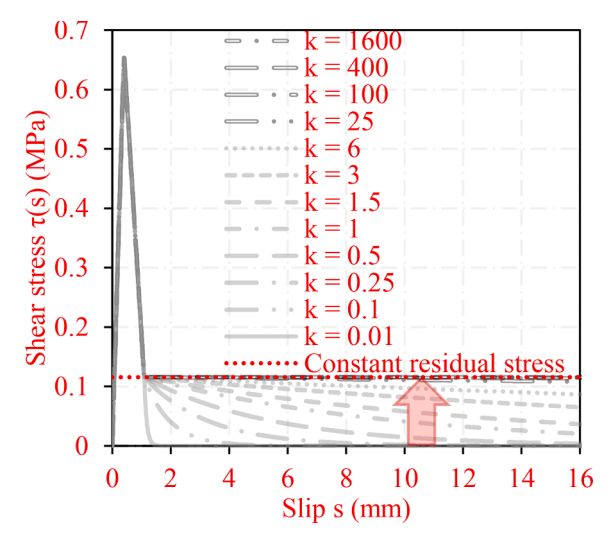


Fig. 6. Parametric study of effect of k to the debonding stage of cohesive interface law. ($s_f = 1.092$ mm; $\tau_f = 0.1158$ MPa; $\alpha = 0.3689$; $\beta = 5.6786$).

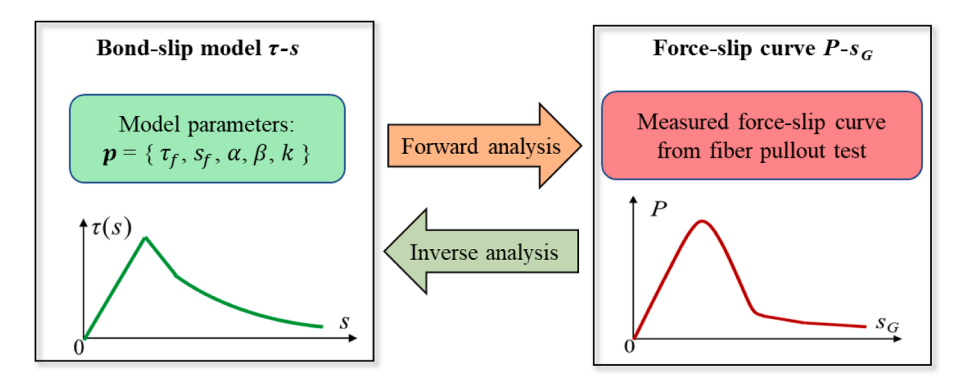


Fig. 7. Comparison of the forward and inverse problems of the fiber pullout behavior.

analysis. The calculation results are compared with the fiber pullout test results. The discrepancy between the calculation results and test results are obtained, and the hypotrochoid spiral algorithm is used to minimize the discrepancy by optimizing the model parameters. The objective function in the minimization is defined as f(X):

$$f(X) = \frac{1}{n} \sum_{i=1}^{n} \text{RMSE}(P(\ell_i, X), Y_i(s_{Gi}))$$

$$\tag{9}$$

where X is the vector composed of the five parameters of CIL; the fiber embedded in the matrix is divided into n segments, and ℓ_i is the i-th length; $P(\ell_i, X)$ is the calculated pullout force corresponding to ℓ_i ; s_{Gi} is the slip corresponding to ℓ_i ; Y_i is a fitted model to estimate the magnitude of the tested pullout force; and the root mean square error (RMSE) is defined as:

RMSE
$$(P, Y_i) = \sqrt{\frac{\sum_{i=1}^{n} (p_i - \nu_i)^2}{n}}$$
 (10)

where $P = [p_1, p_2, ..., p_N]$ and $A = [\nu_1, \nu_2, ..., \nu_N]$ are the vectors for the calculated and tested values of the pullout forces, respectively.

The coefficient of determination (R^2) and the maximum absolute error (MAE) are also used to evaluate the accuracy of the inverse analysis:

$$R^{2} = 1 - \frac{\sum_{i=1}^{n} (p_{i} - \nu_{i})^{2}}{\sum_{i=1}^{n} [\nu_{i} - \text{mean}(\nu_{i})]^{2}}$$
(11a)

MAE
$$(P, Y_i) = \frac{1}{n} \sum_{i=1}^{n} |p_i - \nu_i|$$
 (11b)

The optimization algorithm was executed for 20 independent runs. The number of search agents was set to 50, and the optimization process was terminated when the number of iterations reached 500. More details of the optimization algorithm are available in references [33,34]. After parameters α , β , τ_f , s_f , and k are determined through the inverse analysis, the CIL is determined and used to derive the force-slip curve, the slip distribution and shear stress distribution at the fiber–matrix interface, as well as the axial strain distribution of the fiber at an arbitrary slip level.

2.4. Distributed fiber optic sensing

Distributed fiber optic strain sensors have been categorized into Brillouin scattering-based sensors and Rayleigh scattering-based sensors. Brillouin scattering is a type of inelastic scattering involving frequency shift caused by the interaction of sound waves and light waves [35]. Rayleigh scattering is elastic because it retains the frequency of transmitted light. Rayleigh scattering is caused by irregular microstructures [36]. The irregularity is generated in fiber fabrication, and the irregularity size is comparable with wavelengths of light waves. Compared with Rayleigh scattering, Brillouin scattering features a long operation distance and a low spatial resolution. The resolution of Brillouin optical time domain analysis is about a half meter [5], leading to uncertainties in the measurement of strains. Rayleigh scattering-based sensing technologies were proposed to achieve sub-millimeter spatial resolutions [11,12,37]. With fine spatial resolution, distributed sensors are able to locate and quantify fine strain distributions and cracks [10–12].

In this research, a distributed fiber optic sensing system (model: Luna ODiSi 6100 series) based on the optical frequency domain reflectometry (OFDR) technology was adopted for strain measurements. The manufacturer-specified accuracy is \pm 5 $\mu\epsilon$ [38]. The measurement of strain and temperature is based on the comparison of scattering signals at the reference and perturbed states. In each state, a light wave is beamed into the optical fiber, generating Rayleigh scattering. The backscattered signal is measured along the fiber

length. At each point of the fiber, the amplitude of the signal is plotted against the wavelength of the light. The amplitude versus wavelength data is converted into intensity versus frequency via Fast Fourier Transform, and a cross-correlation operation is performed to identify frequency shift between the reference and the perturbed states at each spot along the fiber. The distance is determined by the travelling time of the backscattered signals because the velocity of light waves can be calculated with the refractive index of the fused silica fiber. The frequency shift is associated with strain and temperature changes:

$$\frac{\Delta\lambda}{\lambda} = \frac{\Delta v}{p} = K_T T + K_\varepsilon \varepsilon \tag{12}$$

where λ and ν are the mean optical wavelength and frequency, and K_T and K_ε are the temperature and strain calibration constants, respectively. At a constant temperature, the spectral shift can be converted into strain along the optical fiber with a calibrated sensitivity coefficient. See calibration in reference [8]. More details of the working principle of the distributed fiber optic sensing system are available in references [11,12].

3. Analytical studies

Previous research showed that the fiber pullout process and the failure mode were dependent on the fiber length (ℓ) embedded in the matrix, and there was a critical embedment length (ℓ ₀) for the fiber [18,32]. The critical embedment length is the minimum length necessary to completely activate the whole CIL along embedded fiber length (ℓ) in the matrix.

Based on the critical embedment length (ℓ_0), the pullout behavior is investigated in two cases: (1) Case 1: the embedment length is longer than the critical length ($\ell > \ell_0$). The pullout process in Case 1 included five stages, which are the elastic stage, elastic-yielding stage, elastic-yielding-debonding stage, yielding-debonding stage, and debonding stage. (2) Case 2: the embedment length is shorter than the critical length ($\ell < \ell_0$). The pullout process in Case 2 included five stages, which are the elastic stage, elastic-yielding stage, yielding-debonding stage, and debonding stage. The difference between the two cases is that the elastic-yielding-debonding stage in Case 1 is replaced by the yielding stage in Case 2. Section 3.1 elaborates the analysis for Case 1. Section 3.2 elaborates the analysis for Case 2.

Long embedment lengths enable the complete development of the interface capacity, and the snap-back behavior only occurs for long embedment lengths. Short embedment lengths undergo lower strain and load levels. Therefore, it is essential to evaluate the critical embedment length ℓ_0 , considering that the failure mode of the fiber pullout test is fiber slip. The five main stages of the fiber–matrix interface damage in the fiber pullout process are shown in Fig. 8. The mechanical behavior is related to the bond length (ℓ), which is the embedment length of the optical fiber in the matrix. More details of the critical embedment length are provided in the following section.

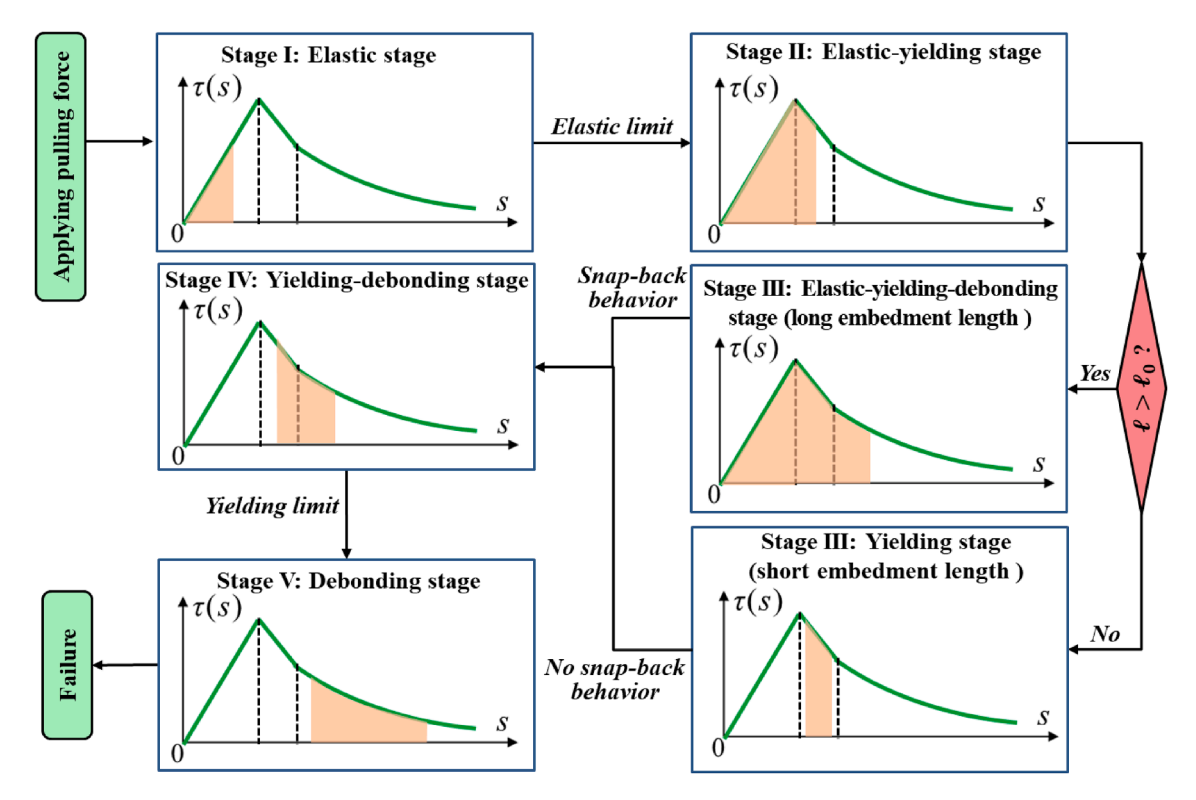


Fig. 8. Illustration of the main stages of the fiber-matrix damage in the single fiber pullout process.

IV

Table 2 Analytical solutions for long embedment length ($\ell > \ell_0$).

Stage	Analytical solutions	
	$s(x) = s_F \cosh(\lambda_1 x)$	(13a)
	$\tau(x) = \frac{\beta \tau_f}{\alpha s_f} s_F \cosh(\lambda_1 x)$	(13b)
	$arepsilon_f(x) = rac{1}{\omega} \lambda_1 s_F \mathrm{sinh}(\lambda_1 x)$	(13c)
I	The solution at the region of $0 \le x \le \ell_{el}$:	
	$s(x) = as_f \frac{\cosh(\lambda_1 x)}{\cosh(\lambda_1 x_d)}$	(14a)
	$\tau(x) = \beta \tau_{f} \frac{\cosh(\lambda_1 x)}{\cosh(\lambda_1 x')}$	(14b)
	$\varepsilon_f(x) = \frac{1}{a} \lambda_1 a s_f \sinh(\lambda_1 x)$	(14c)
	φ $\cos(\lambda_1 \ell_{el})$ The solution at the region of $\ell_{el} \le x \le \ell$:	
	$s(x) = \begin{cases} \frac{(1-\alpha)\beta s_f}{1-\beta} \cosh[\lambda_2(\ell_{el}-x)] - \frac{\lambda_1 \alpha s_f}{\lambda_2} \tanh(\lambda_1 \ell_{el}) \sinh[\lambda_2(\ell_{el}-x)] - \frac{\beta-\alpha}{1-\beta} s_f, \beta \neq 1 \\ \frac{1}{2} \lambda^2 \tau_f(\ell_{el}-x)^2 - \lambda_1 \alpha_f \tanh(\lambda_1 \ell_{el}) \bullet (\ell_{el}-x) + \alpha s_f, \beta = 1 \end{cases}$	(14d)
	$\frac{1}{2}\lambda^2\tau_f(\ell_{el}-x)^2 - \lambda_1\alpha_f \mathrm{tanh}(\lambda_1\ell_{el}) \bullet (\ell_{el}-x) + \alpha s_f, \beta = 1$	
	$\tau(x) = \begin{cases} \beta \tau_f \mathrm{cosh}[\lambda_2(\ell_{el} - x)] - \frac{\alpha(1 - \beta)\lambda_1 \tau_f}{(1 - \alpha)\lambda_2} \tanh(\lambda_1 \ell_{el}) \sinh[\lambda_2(\ell_{el} - x)], \beta \neq 1 \\ \tau_f, \beta = 1 \end{cases}$	(14e)
	$\left(\frac{1}{\omega}\lambda_{1}\alpha s_{f} \tanh(\lambda_{1}\ell_{el})\cosh[\lambda_{2}(\ell_{el}-x)] - \frac{1}{\omega}\lambda_{2}\frac{(1-\alpha)\beta s_{f}}{1-\beta}\sinh[\lambda_{2}(\ell_{el}-x)], \beta \neq 1\right)$	(14f)
	$\varepsilon_f(x) = \begin{cases} \frac{1}{\varphi} \lambda_1 \alpha s_f \tanh(\lambda_1 \ell_{el}) \cosh[\lambda_2 (\ell_{el} - x)] - \frac{1}{\varphi} \lambda_2 \frac{(1 - \alpha)\beta s_f}{1 - \beta} \sinh[\lambda_2 (\ell_{el} - x)], \beta \neq 1 \\ -\frac{1}{\varphi} \lambda^2 \tau_f (\ell_{el} - x) + \frac{1}{\varphi} \lambda_1 \alpha_f \tanh(\lambda_1 \ell_{el}), \beta = 1 \end{cases}$	
III	The solution at the region of $0 \le x \le \ell_{el}$:	
	$s(x) = \alpha s_f \frac{\cosh(\lambda_1 x)}{\cosh(\lambda_1 x)}$	(15a)
	$\tau(x) = \beta \tau_{f} \frac{\cosh(\lambda_1 x)}{\cosh(\lambda_1 x_1)}$	(15b)
	(A)	(15c)
	$arepsilon_f(x) = rac{1}{arphi} \lambda_1 lpha s_f rac{\sinh(\lambda_1 x)}{\cosh(\lambda_1 \ell_{el})}$	(===)
	The solution at the region of $\ell_{el} \le x \le \ell_{el} + \ell_{yd}$:	(15.1)
	$s(x) = \begin{cases} \frac{(1-\alpha)\beta s_f}{1-\beta} \frac{\sinh\left[\lambda_2(\ell_{el}+\ell_{yd}-x)\right]}{\sinh(\lambda_2\ell_{yd})} - \frac{(1-\alpha)s_f}{1-\beta} \frac{\sinh[\lambda_2(\ell_{el}-x)]}{\sinh(\lambda_2\ell_{yd})} - \frac{\beta-\alpha}{1-\beta}s_f, \beta \neq 1 \\ \frac{1}{2}\lambda^2 \tau_f(\ell_{el}-x)(\ell_{el}+\ell_{yd}-x) - \frac{(1-\alpha)s_f}{\ell_{yd}}(\ell_{el}-x) + \alpha s_f, \beta = 1 \end{cases}$	(15d)
	$\frac{1}{2}\lambda^2\tau_f(\ell_{el}-x)\big(\ell_{el}+\ell_{yd}-x\big)-\frac{(1-\alpha)s_f}{\ell_{vd}}(\ell_{el}-x)+\alpha s_f,\beta=1$	
	$\tau(\mathbf{x}) = \begin{cases} \beta \tau_f \frac{\sinh\left[\lambda_2\left(\ell_{el} + \ell_{yd} - \mathbf{x}\right)\right]}{\sinh\left(\lambda_2\ell_{yd}\right)} - \tau_f \frac{\sinh\left[\lambda_2\left(\ell_{el} - \mathbf{x}\right)\right]}{\sinh\left(\lambda_2\ell_{yd}\right)}, \beta \neq 1 \\ \tau_f \beta = 1 \end{cases}$	(15e)
	ij, p=1	(150
	$\varepsilon_f(\mathbf{x}) = \begin{cases} -\frac{1}{\varphi} \lambda_2 \frac{(1-\alpha)\beta s_f}{1-\beta} \frac{\cosh\left[\lambda_2 \left(\ell_{el} + \ell_{yd} - \mathbf{x}\right)\right]}{\sinh\left(\lambda_2 \ell_{yd}\right)} + \frac{1}{\varphi} \lambda_2 \frac{(1-\alpha)s_f}{1-\beta} \frac{\cosh\left[\lambda_2 \left(\ell_{el} - \mathbf{x}\right)\right]}{\sinh\left(\lambda_2 \ell_{yd}\right)}, \beta \neq 1 \end{cases}$	(15f)
	' 1 1 1 1 (1 m)c	

$$s(x) = \frac{2k}{\tau_c} \ln\left\{\cosh\left[\lambda_3 \sqrt{C_1} \left(x - C_2\right)\right]\right\} - \frac{k}{\tau_c} \ln(C_1)$$
(15 g)

$$\varepsilon_{f}(x) = \begin{cases}
-\frac{1}{\varphi} \lambda^{2} \tau_{f}(\ell_{el} - x) - \frac{1}{2} \frac{1}{\varphi} \lambda^{2} \tau_{f}(\ell_{yd} + \varphi \frac{(1 - \alpha)s_{f}}{\ell_{yd}}), \beta = 1 \\
\text{The solution at the region of } \ell_{el} + \ell_{yd} \le x \le \ell; \\
s(x) = \frac{2k}{\tau_{f}} \ln \left\{ \cosh \left[\lambda_{3} \sqrt{C_{1}} (x - C_{2}) \right] \right\} - \frac{k}{\tau_{f}} \ln(C_{1})
\end{cases} \tag{15 g}$$

$$\tau(x) = \frac{C_{1} \tau_{f} \bullet e}{\cosh \left[\lambda_{3} \sqrt{C_{1}} (x - C_{2}) \right]}$$

$$\tau(x) = \frac{C_{1} \tau_{f} \bullet e}{\cosh \left[\lambda_{3} \sqrt{C_{1}} (x - C_{2}) \right]}$$

$$\tau(x) = \frac{1}{2k} \sqrt{C_{1}} \left[\lambda_{3} \sqrt{C_{1}} \left(x - C_{2} \right) \right]$$

$$\tau(x) = \frac{1}{2k} \sqrt{C_{1}} \left[\lambda_{3} \sqrt{C_{1}} \left(x - C_{2} \right) \right]$$
(15i)

$$\varepsilon_f(\mathbf{x}) = \frac{1}{\varphi} \frac{2k}{\tau_f} \lambda_3 \sqrt{C_1} \tanh \left[\lambda_3 \sqrt{C_1} \left(\mathbf{x} - C_2 \right) \right] \tag{15i}$$

$$s(x) = \begin{cases} \frac{1-\alpha}{1-\beta} s_f \frac{\cosh(\lambda_2 x)}{\cosh(\lambda_2 \ell_{yd})} - \frac{\beta-\alpha}{1-\beta} s_f, \beta \neq 1\\ \frac{1}{\alpha} \lambda^2 r_f \left(x^2 - \ell_{yd}^2\right) + s_f, \beta = 1 \end{cases}$$
(16a)

$$\tau(x) = \begin{cases} \tau_f \frac{\cosh(\lambda_2 x)}{\cosh(\lambda_2 \ell_{yd})}, \beta \neq 1\\ \tau_f \cdot \beta = 1 \end{cases}$$
(16b)

$$\tau(x) = \frac{1}{\cosh^{2}\left[\lambda_{3}\sqrt{C_{1}}(x - C_{2})\right]} \\
\varepsilon_{f}(x) = \frac{1}{\theta} \frac{2k}{\tau_{f}} \lambda_{3} \sqrt{C_{1}} \tanh\left[\lambda_{3}\sqrt{C_{1}}(x - C_{2})\right] \\
\text{The solution at the region of } 0 \le x \le \ell_{yd}; \\
s(x) = \begin{cases}
\frac{1 - \alpha}{1 - \beta} s_{f} \frac{\cosh(\lambda_{2}x)}{\cosh(\lambda_{2}\ell_{yd})} - \frac{\beta - \alpha}{1 - \beta} s_{f}, \beta \ne 1 \\
\frac{1}{2} \lambda^{2} \tau_{f} \left(x^{2} - \ell_{yd}^{2}\right) + s_{f}, \beta = 1
\end{cases}$$

$$\tau(x) = \begin{cases}
\tau_{f} \frac{\cosh(\lambda_{2}x)}{\cosh(\lambda_{2}\ell_{yd})}, \beta \ne 1 \\
\tau_{f}, \beta = 1
\end{cases}$$

$$\varepsilon_{f}(x) = \begin{cases}
\frac{1}{\phi} \lambda_{1}^{2} \frac{1 - \alpha}{\beta} s_{f} \frac{\sinh(\lambda_{2}x)}{\cosh(\lambda_{2}\ell_{yd})}, \beta \ne 1 \\
\frac{1}{\phi} \lambda^{2} \tau_{f}x, \beta = 1
\end{cases}$$
The solution at the region of $\ell_{yd} \le x \le \ell$:

The solution at the region of $\ell_{yd} \le x \le \ell$:

(continued on next page)

Table 2 (continued)

Stage	Analytical solutions	
I	$s(x) = s_F \cosh(\lambda_1 x)$	(13a)
	$s(x) = \frac{2k}{\tau_f} \ln \left\{ \cosh \left[\lambda_3 \sqrt{C_3} \left(x - C_4 \right) \right] \right\} - \frac{k}{\tau_f} \ln(C_3)$	(16d)
	Tysy Cozona k	(16e)
	$\tau(x) = \frac{C_3 \tau_f \bullet e}{\cosh^2 \left[\lambda_3 \sqrt{C_3} \left(x - C_4 \right) \right]}$	
	$arepsilon_f(x) = rac{1}{arphi} rac{2k}{ au_f} \lambda_3 \sqrt{C_3} anh \Big[\lambda_3 \sqrt{C_3} \left(x - C_4 ight) \Big]$	(16f)
V	$s(x) = \frac{2k}{\tau_f} \ln \left\{ \cosh \left[\lambda_3 \sqrt{C_5} \left(x - C_6 \right) \right] \right\} - \frac{k}{\tau_f} \ln(C_5)$	(17a)
	$\tau(x) = \frac{C_5 \tau_f \bullet e \frac{\tau_f s_f}{k}}{\cosh^2 \left[\lambda_3 \sqrt{C_5} \left(x - C_6 \right) \right]}$	(17b)
	$\varepsilon_f(x) = \frac{1}{\varphi} E_f \frac{2k}{\tau_f} \lambda_3 \sqrt{C_5} \tanh \left[\lambda_3 \sqrt{C_5} \left(x - C_6 \right) \right]$	(17c)

3.1. Case 1: Long embedment length $(\ell > \ell_0)$

With the CIL in Fig. 4, the governing equation was solved to determine the slip, shear stress, and axial strain distributions along the embedded fiber length, as summarized in Table 2. In Table 2, ℓ_{el} and ℓ_{yd} are the elastic length and the yielding length, respectively, which are determined by the boundary conditions. The constants λ_1 , λ_2 , λ_3 and C_1 to C_6 were used to simplify the formulae. The detailed derivation process of the formulae as well as the expressions of λ_1 , λ_2 , λ_3 and C_1 to C_6 are available in Appendix A1.

The elastic, yielding, and debonding stages simultaneously occur at the fiber-coating interface only when the embedment length (ℓ) is longer than the critical embedment length (ℓ 0) in Eq. (18). The detailed derivation process of Eq. (18) is shown in Appendix A1.

$$\ell_0 = \begin{cases} \frac{1}{\lambda_2} \cosh^{-1}\left(\frac{1}{\beta}\right), \beta \neq 1 \\ \frac{1}{\lambda} \sqrt{\frac{2(1-\alpha)s_f}{\tau_f}}, \beta = 1 \end{cases}$$
(18)

The elastic stage (Stage I) ends when $\tau(\ell) = \beta \tau_f$ (Point A in Fig. 9). The load and the corresponding loaded end slip at the end of the elastic stage are:

$$P_{A} = A_{f} E_{f} \frac{1}{\omega} \lambda_{1} \tanh(\lambda_{1} \ell) \alpha s_{f}$$

$$\tag{19a}$$

$$s_{GA} = \alpha s_f$$
 (19b)

The elastic-yielding stage (Stage II) ends when $\tau(\ell) = \tau_f$ (Point C in Fig. 9). The load and the corresponding loaded end slip at the end of the elastic-yielding stage are:

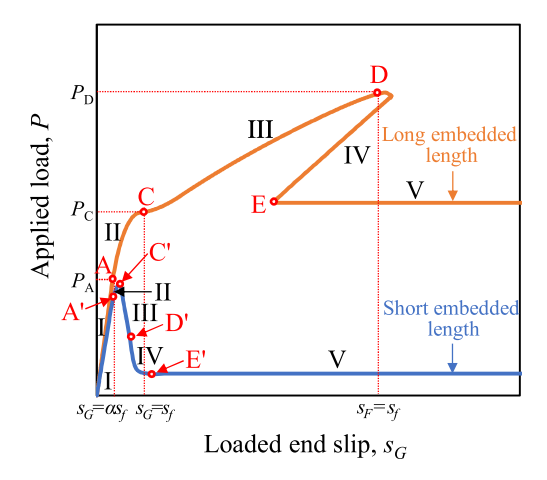


Fig. 9. Analytical load-global slip curves for both long and short embedded lengths.

$$P_{C} = \begin{cases} A_{f}E_{f}\frac{1}{\varphi}\lambda_{2}\frac{(1-\alpha)\beta s_{f}}{1-\beta}\sinh(\lambda_{2}\ell), \beta \neq 1\\ A_{f}E_{f}\frac{1}{\varphi}\lambda^{2}\tau_{f}l, \beta = 1 \end{cases}$$
(20a)

$$s_{G,C} = \begin{cases} \frac{(1-\alpha)\beta s_f}{1-\beta} \cosh(\lambda_2 \ell) - \frac{\beta-\alpha}{1-\beta} s_f, \beta \neq 1\\ \frac{1}{2} \lambda^2 \tau_f \ell^2 + \alpha s_f, \beta = 1 \end{cases}$$
(20b)

The elastic-yielding-debonding stage (Stage III) ends when $\tau(0) = \beta \tau_f$ (Point D in Fig. 9). The load and the corresponding loaded end slip at the end of elastic-yielding-debonding stage are:

$$P_D = A_f E_f \frac{1}{\varphi} \frac{2k}{\tau_f} \lambda_3 \sqrt{C_1} \tanh \left[\lambda_3 \sqrt{C_1} \left(\ell - C_2 \right) \right], \\ (\text{when} \ell_{yd} = \ell_0)$$
 (21a)

$$s_{G,D} = \frac{2k}{\tau_f} \ln \left\{ \cosh \left[\lambda_3 \sqrt{C_3} \left(\ell - C_4 \right) \right] \right\} - \frac{k}{\tau_f} \ln(C_3), (\text{when} \ell_{yd} = \ell_0)$$
(21b)

The yielding-debonding stage (Stage IV) ends when $\tau(0) = \tau_f$ (Point E in Fig. 9). The load and the corresponding loaded end slip at the end of the elastic stage are:

$$P_E = A_f E_f \frac{1}{\varphi} \frac{2k}{\tau_f} \lambda_3 e^{-\left(\frac{\gamma_f y}{2k}\right)} \tanh\left(\lambda_3 e^{-\left(\frac{\gamma_f y}{2k}\right)} \ell\right)$$
 (22a)

$$s_{G,E} = \frac{2k}{\tau_f} \ln \left[\cosh \left(\lambda_3 e^{-\left(\frac{f_2 f_1}{2k} \right)} \ell \right) \right] + s_f$$
 (22b)

3.2. Case 2: Short embedment length ($\ell < \ell_0$)

When the embedment length of fiber is shorter than the critical embedment length ($\ell < \ell_0$), the elastic-yielding-debonding stage in Case 1 is replaced by a yielding stage. The other stages in Cases 1 and 2 are the same, so they are not duplicated. This section only elaborates the yielding stage (Stage III), and the corresponding formulae of slip, shear stress, and axial strain distributions along the embedded fiber length are summarized in Table 3. The detailed derivation process of the formulae is available in Appendix A2.

The yielding stage (Stage III) is ended when $s_{GD} = s_f$. The corresponding load at the end of the yielding stage is:

$$P_{D} = \begin{cases} \varphi A_{f} E_{f} \left(\frac{1-\alpha}{1-\beta} \right) s_{f} \lambda_{2} \tanh(\lambda_{2} \ell), \beta \neq 1 \\ \varphi A_{f} E_{f} \lambda^{2} \tau_{f} I, \beta = 1 \end{cases}$$
(24)

3.3. Analytical results

As discussed in Section 3.1, five stages are identified from the load response of an optical fiber when the fiber embedded length is longer than the critical embedded length: (I) elastic; (II) elastic-softening; (III) elastic-softening-debonding; (IV) softening-debonding; and (V) debonding stages. These stages are shown in orange color in Fig. 9. A snap-back phenomenon is observed, although it is usually not captured in laboratory experiments due to the adopted testing method which is either force or displacement that is controlled to increase monotonically [17,18]. More discussions on the snap-back phenomenon are available in references [17,18]. The snap-back

Table 3 Analytical solutions for short embedment length ($\ell < \ell_0$).

Stage III	Analytical solutions $s(x) = \begin{cases} \left(s_F + \frac{\beta - \alpha}{1 - \beta}s_f\right) \cosh(\lambda_2 x) - \frac{\beta - \alpha}{1 - \beta}s_f, \beta \neq 1 \\ \frac{1}{2}\lambda^2 \tau_f x^2 + s_F, \beta = 1 \end{cases}$	(23a)
	$ au(\mathbf{x}) \ = \left\{ egin{array}{l} rac{[(1-eta) au_{\!f}}{(1-lpha)s_{\!f}}s_{\!F} + rac{eta-lpha}{1-lpha} au_{\!f} big] \cosh(\lambda_2\mathbf{x}), eta eq 1 \ & au_{\!f}, eta = 1 \end{array} ight.$	(23b)
	$arepsilon_f(\mathbf{x}) = \left\{egin{align*} & arphi_1, & arphi = 1 \ & arphi_2 \left(s_F + rac{eta - lpha}{1 - eta} s_f ight) \sinh(\lambda_2 \mathbf{x}), eta eq 1 \ & arphi^2 au_f \mathbf{x}, eta = 1 \end{array} ight.$	(23c)

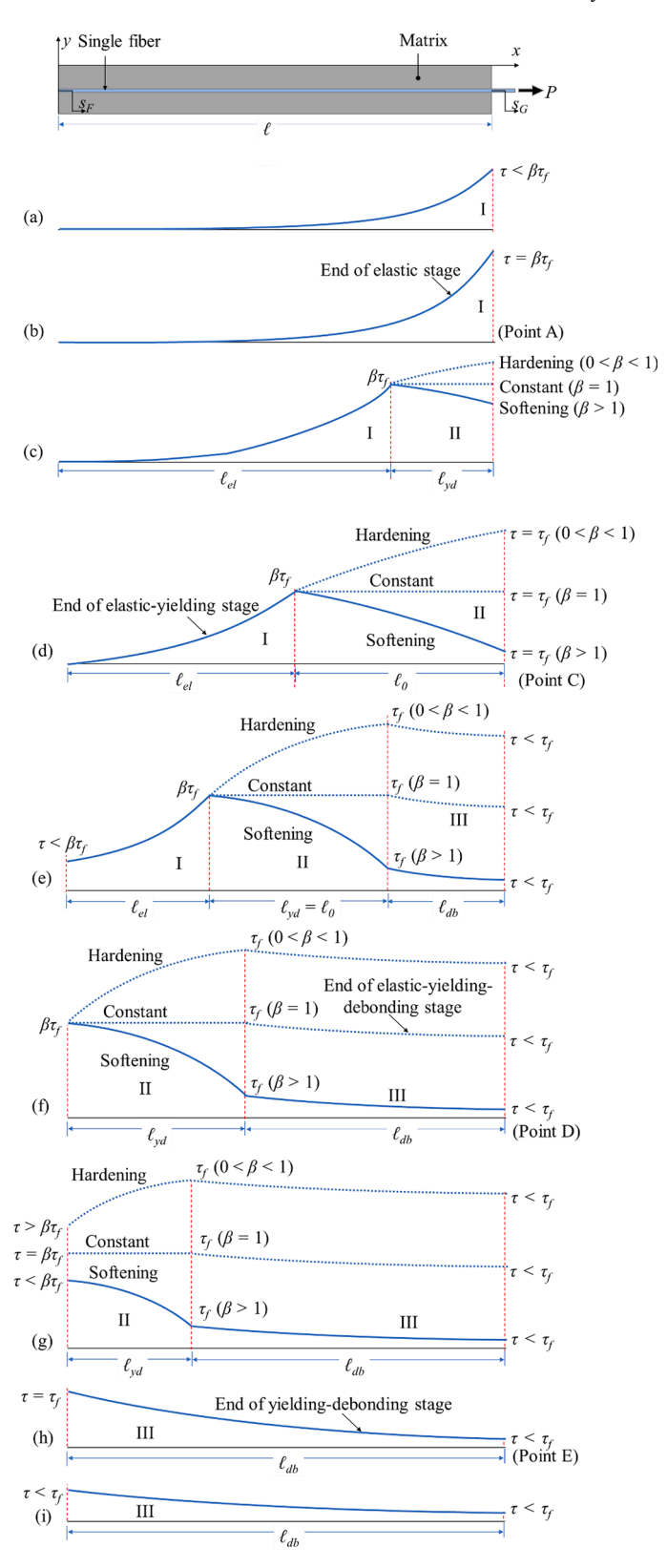


Fig. 10. Evolution of interfacial shear stresses for a long embedment length: (a, b) elastic stage; (c, d) elastic-yielding stage; (e, f) elastic-yielding debonding stage; (g, h) yielding-debonding stage; and (i) debonding stage. I, II and III are elastic, yielding and debonding stress states, respectively.

phenomenon is usually more interesting to research focusing on the mechanical properties of composites, but it is not the main focus of this research, which mainly focuses on the sensing performance of distributed fiber optic sensors.

When the fiber embedded length is shorter than the critical embedded length, the load response of an optical fiber also can be divided into five stages, shown in blue color in Fig. 9. The curve is a typical fiber pullout curve showing a softening trend.

Based on the unified CIL and analytical solutions, the shear stress distributions along the interface are obtained by solving the governing equation at each loading stage. Fig. 10 illustrates the evolution of the interfacial shear stress when the embedment length is longer than the critical embedment length ($\ell > \ell_0$).

The evolution of the interfacial shear stresses for a long embedment length is characterized by five stages. In the first stage, the load–displacement response is linear elastic. The shear stress distributions along the interface are shown in Fig. 10(a) and Fig. 10(b). At the end of the elastic stage, a portion of the interface enters the yielding stage, while the remaining portion is still in the elastic stage. The corresponding shear stress distributions along the interface are depicted in Fig. 10(c) and Fig. 10(d). Specifically, the parameter β has a significant effect on the shear stress distribution. When $\beta > 1$, the shear stress distribution shows a softening effect for the portion of interface in the yielding stage; when $\beta = 1$, the shear stress distribution is constant; and when $0 < \beta < 1$, the shear stress distribution shows a hardening effect. At the end of the elastic-yielding stage, a portion of the interface enters the debonding stage, while the remaining part is still in the elastic-yielding stage. The corresponding shear stress distributions along the interface are depicted in Fig. 10(e) and Fig. 10(f). In the elastic-yielding-debonding stage, the applied force increases due to the debonding at the interface. At the end of the elastic-yielding-debonding stage, there is no elastic stage at the interface. The shear stress distributions are shown in Fig. 10(g) and Fig. 10(h). At the end of the yielding-debonding stage, the shear stress is equal to the bond strength (τ_f) at the free end. Finally, Fig. 10(i) depicts the shear stress distribution at debonding stage.

When the embedment length is shorter than the critical embedment length ($\ell < \ell_0$), the shear stress distribution at the end of the elastic-debonding stage is shown in Fig. 11(a). There is no elastic stage along the fiber, and the interface is in the softening stage along the whole fiber length. At the end of the softening phase, the shear distribution is shown in Fig. 11(b). Then, the shear stress distribution evolves to the yielding-debonding stage.

4. Implementation

The presented interface law and analysis is implemented into optical fibers that were used to validate the approaches. Validation of the approaches took advantage of the unique sensing capability of the distributed fiber optic sensors. The proposed CIL and the derivation of the analytical formulae (see Section 3 and Appendix A) are independent of the specific materials (optical fibers) and applicable to different types of composites.

4.1. Pullout tests

Single fiber pullout tests were carried out as shown in Fig. 12(a). In each test, an optical fiber was attached using adhesive (ethyl cyanoacrylate super glue) on two aluminum plates (length \times width \times thickness: 200 mm \times 30 mm \times 5 mm). Two U-shape channels were used as slideways to regulate the deformation of the aluminum plates. With the U-shape channels, the aluminum plates could only slide along the channels along the length direction, which is also the loading direction, and there was no out-of-plane deformation or torsion of the aluminum plates. Before the loading test, the two aluminum plates were in direct contact with each other, and they were attached together by using a drop of super glue. The optical fiber was glued to the surface of the aluminum plates along the length

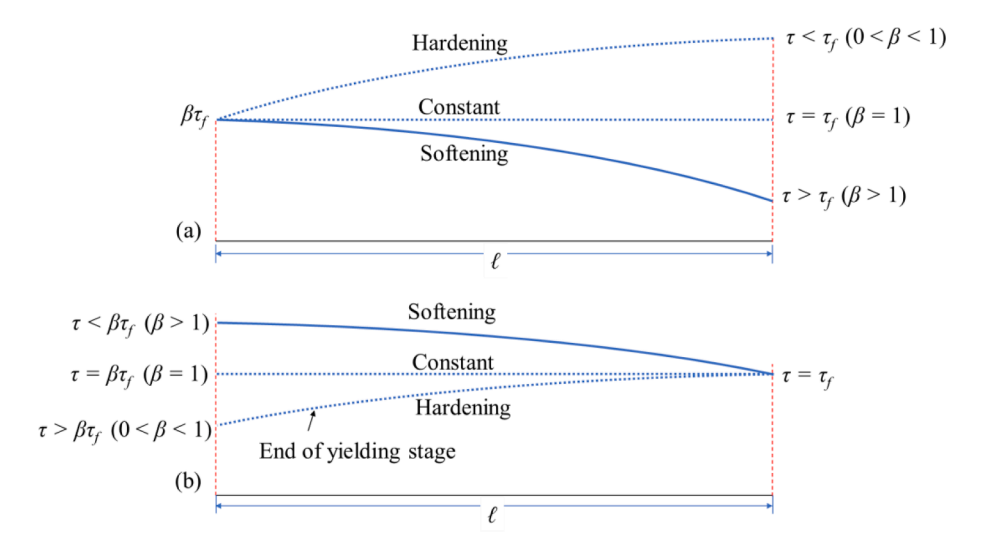


Fig. 11. Evolution of interfacial shear stress distribution of yielding stage for a short embedment length and propagation of debonding.

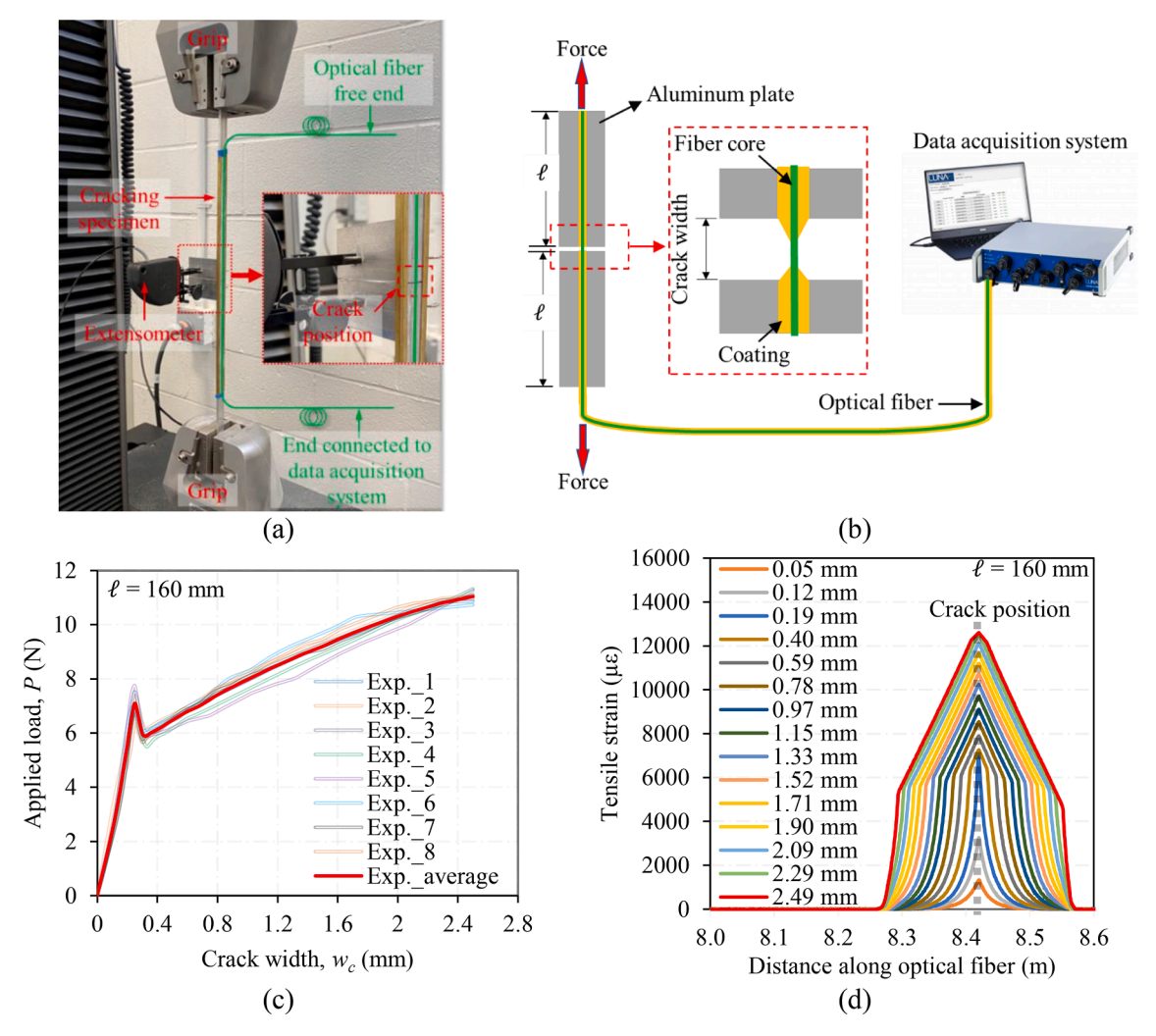


Fig. 12. Fiber pullout test: (a) photograph of the test set-up; (b) illustration of the test set-up; (c) representative pullout load versus crack width curves; and (d) representative experimental strain distribution curves with crack width opening. "Exp." represents the experimental results.

direction and passed through the joint of the two aluminum plates. The joint was used to simulate an artificial crack that was perpendicular to the optical fiber, as shown in Fig. 12(b). One end of the optical fiber was connected to the distributed data acquisition system for measuring the strain distributions along the optical fiber, and the other end of the optical fiber was free. The two ends of the aluminum plate were gripped by the wedges of a low-capacity load frame (load capacity: 1 kN; accuracy: $\pm 0.2 \text{ N}$) to apply tensile forces to the specimen. The embedment fiber length with the coating was $\ell=160 \text{ mm}$ at each aluminum plate. The test was repeated eight times. The fused silica fiber was pulled under displacement control at a constant rate of 0.5 mm/min. The applied force was measured from the load cell embedded in the load frame. An extensometer measured the relative displacement between the two aluminum plates representing the crack width increase.

Representative results are shown in Fig. 12(c). The pullout curves indicate a transition behavior, which can be attributed to the occurrence of debonding in the optical fiber. When the crack widths about 0.3 mm, the trend of the curve is significantly changed, because the strain transfer behavior between the matrix and the optical fiber is altered after debonding occurs. The small load drop near the transition joint is attributed to the loading rate (0.5 mm/min), because it is difficult for the load frame to accurately react to the sudden occurrence of interface debonding in pullout process. Fig. 12(d) shows the representative strain distribution curves with crack width opening. The peak indicates the location of the crack. The strain distributions are almost symmetrical to the peak. The development of the strain distribution is consistent with pullout curves. When the crack width is increased from 0 to 0.19 mm, the corresponding strain distribution shows a sharp peak at the location of the crack, indicating the crack initiation. When the crack width is larger than 0.4 mm, the strain peak is widened with the increase of the crack width due to debonding in the optical fiber, and the abrupt elongation of the optical fiber at the crack was averaged over a longer length, reducing the peak strain. The debonding length then propagates along the fiber length. Eventually, after the debonding length is significantly developed, the distributed sensor fails to provide further measurement.

4.2. Metaheuristic inverse analysis

The model parameters α , β , τ_f , s_f , and k were determined through the metaheuristic inverse analysis based on the fiber pull-out test results. Fig. 13 shows the optimization convergence curves for the 20 independent runs of the inverse analysis. The curves indicate that the adopted algorithm effectively minimizes the objective function and avoids premature convergence. Table 4 lists the results of the parameters of the CIL and performance metrics. The results indicate that the force-slip results obtained from the inverse analysis agree with the test results. Fig. 14(a) compares the experimental and analytical results of the force-crack width curves based on inverse analysis.

4.3. Distributed fiber optic sensing

With the model parameters, the mechanical model was used to derive the slip distribution and the shear stress distribution at the fiber-coating interface and the strain distribution in the fiber along the fiber length at an arbitrary crack width opening. Fig. 14(a) plots nine selected crack width levels at the loaded end, $w_c = [0.05 \text{ mm}, 0.12 \text{ mm}, 0.22 \text{ mm}, 0.32 \text{ mm}, 0.59 \text{ mm}, 0.78 \text{ mm}, 1.33 \text{ mm}, 1.89 \text{ mm}, 2.49 \text{ mm}]$, in the pullout force-crack width curve when the embedment length is 160 mm. The nine crack width levels were selected to represent nine stages of the pullout process. This analytical analysis provides a theoretical foundation for measuring the crack widths using the empirical relationship between the magnitude of strain peak measured from distributed fiber optic sensors and crack width, as elaborated in reference [11].

Fig. 14(b) compares the analysis results of the strain distributions in the fused silica fiber against the measurement results from the distributed fiber optic sensor based on OFDR. The analysis and measurement results of the strain distributions agree, indicating that the presented interface law and inverse analysis are effective in analyzing the interfacial behavior of the fused silica fiber with the package. The gained understanding of the interfacial behavior enables the operation of distributed fiber optic sensors and the interpretation of the sensing data in the presence of debonding at the fiber-coating interface. In the presence of cracks, the theoretical formula that relates the slip of the optical fiber and the crack opening width is determined according to the governing equation Eq. (5), and the crack width is calculated by the integration of the tensile strains in the vicinity of the crack. This analytical analysis also paves the theoretical way to quantifying the crack widths using the strain distributions measured from distributed fiber optic sensors, as elaborated in reference [11]. The developed approaches enable accurate interpretation of the results from the distributed fiber optic sensors.

Fig. 14(c) shows the slip distributions along the fiber length at different crack width openings. The slip reaches the maximum value at the loaded end ($x = \ell$) and gradually decreases towards the free end (x = 0) of the fiber. When the slip is small ($s_G < 0.284$ mm or $w_c < 0.12$ mm), the entire interface is elastic. When s_G increases from 0.284 mm to 1.746 mm (or 0.12 mm $< w_c < 0.59$ mm), the interface is in the elastic-yielding stage. When s_G increases from 1.746 mm to 7.310 mm (or 0.59 mm $< w_c < 2.49$ mm), the fiber corecladding interface is in the elastic-yielding-debonding stage.

Fig. 14(d) shows the shear stress distributions along the fiber length at different crack width openings. When the crack width opening is small ($w_c < 0.12$ mm), the shear stress reaches the maximum value at the loaded end and gradually decreases towards the free end of the fiber. When the crack width opening increases from 0.12 mm to 0.59 mm, the maximum shear stress reaches the peak shear, the maximum shear stress reaches the peak at the intersection between the elastic and yielding sections. The position of maximum shear stress moves toward the free end of the embedded section when the crack width opening increases. When the crack width opening is larger than 0.59 mm, the loaded end of the embedded section reaches the debonding section, and the position of peak shear stress moves further toward the free end of the embedded fiber.

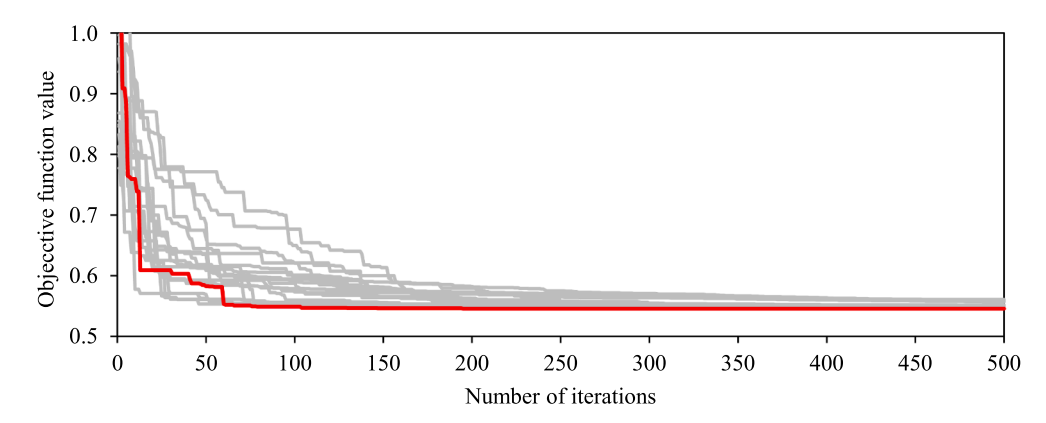


Fig. 13. Convergence curves of the hypotrochoid spiral optimization algorithm for 20 independent runs. The red line represents the best result, and the gray lines represent the other results. (For interpretation of the references to color in this figure legend, the reader is referred to the web version of this article.)

Table 4 Parameters of the bond-slip relationships.

Samples (/ = 160 mm)	s _f (mm)	$ au_f(ext{MPa})$	α	β	k(N/mm)	RMSE	\mathbb{R}^2	MAE
Exp1	1.092	0.1158	0.3689	5.6786	1621.54	0.1225	0.984	0.0901
Exp2						0.1032	0.991	0.0715
Exp3						0.1009	0.994	0.0791
Exp4						0.1102	0.992	0.0804
Exp5						0.1231	0.995	0.1002
Exp6						0.1068	0.987	0.0787
Exp7						0.1242	0.993	0.1013
Exp8						0.1097	0.989	0.0925
Expaverage						0.1125	0.991	0.0867

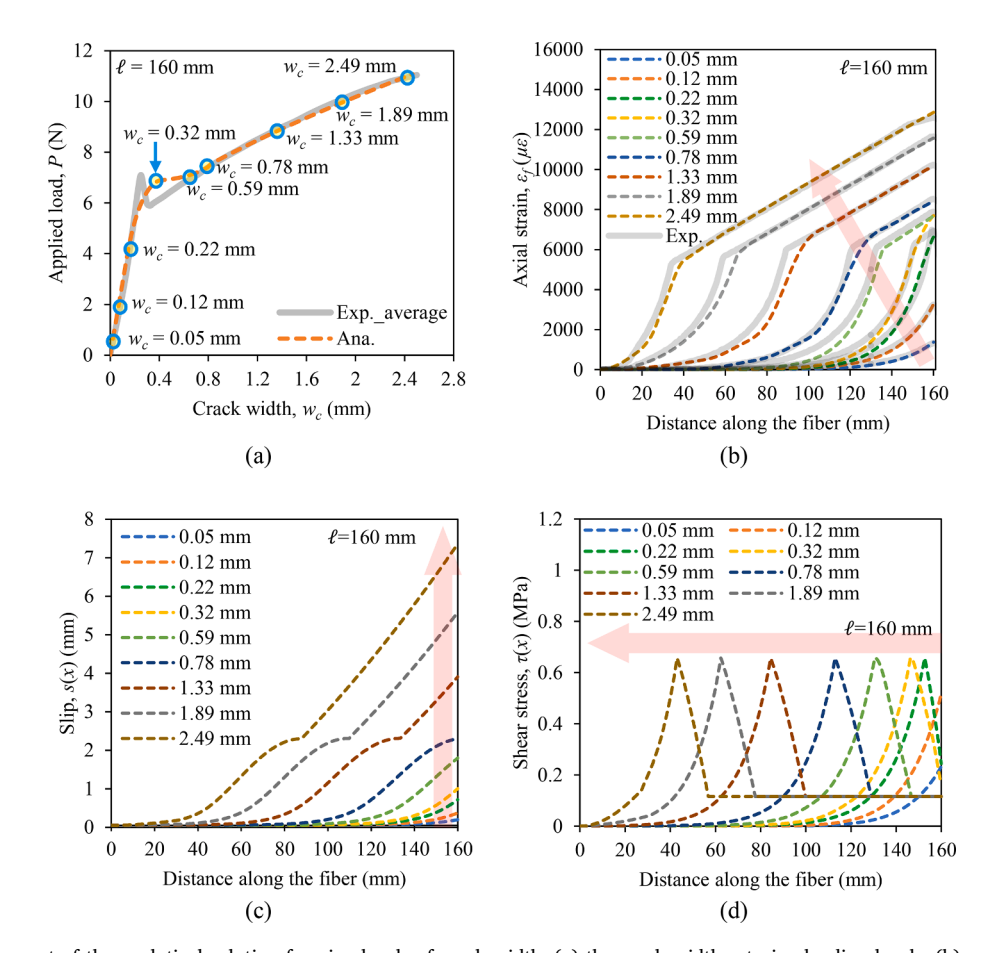


Fig. 14. Assessment of the analytical solution for nine levels of crack width: (a) the crack widths at nine loading levels; (b) comparison of the analytical and experimental results of axial strain distributions; (c) slip distributions; and (d) shear stress distributions. "Exp." and "Ana." represent the experimental results and the analytical results, respectively.

4.4. Discussion on unsymmetrical cases

The former investigations on the relationship between fiber end slip and crack width were built on an assumption that an optical fiber crossing a crack experiences symmetrical loaded end slips. However, that is not always the case. In general, the loaded end slips of the fiber at the two sides of the crack are unequal due to the randomness of material properties. This section discusses the unsymmetrical case, as shown in Fig. 15. When the right side of the fiber enters the debonding stage (Stage 3 in Fig. 5), the left side of the fiber is still in the yielding stage (Stage 2 in Fig. 5). Under such circumstances, it is inappropriate to use the fiber end slip at one side of the crack to calculate the crack width. The fiber end slips at both the left and right sides of the crack should be used, and the crack width w_c is equal to the sum of the loaded end slips of the left and right sides, which are denoted as w_L and w_R , respectively, according to the compatibility of deformations, as shown in Eq. (25a)-c). According to the equations of equilibrium, Eq. (25d) is obtained.

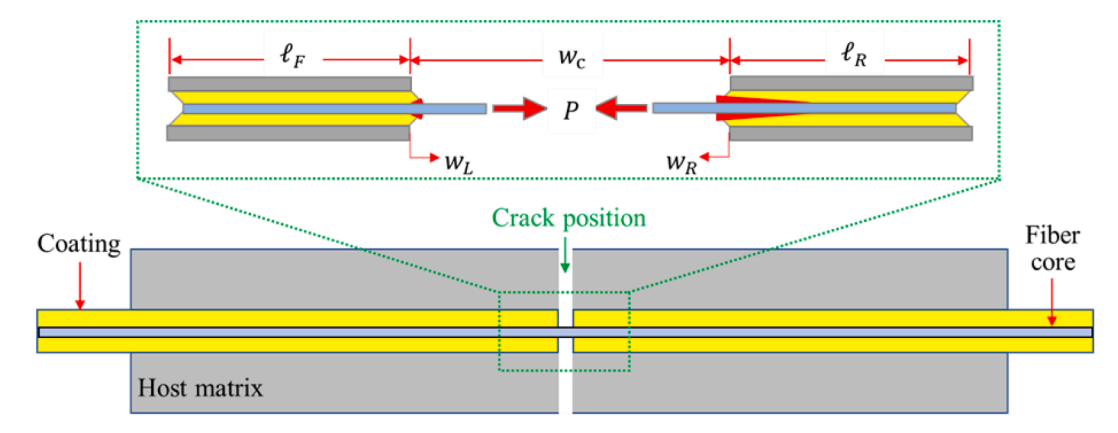


Fig. 15. Illustration of the unsymmetrical fiber pullout cases for determining the crack width.

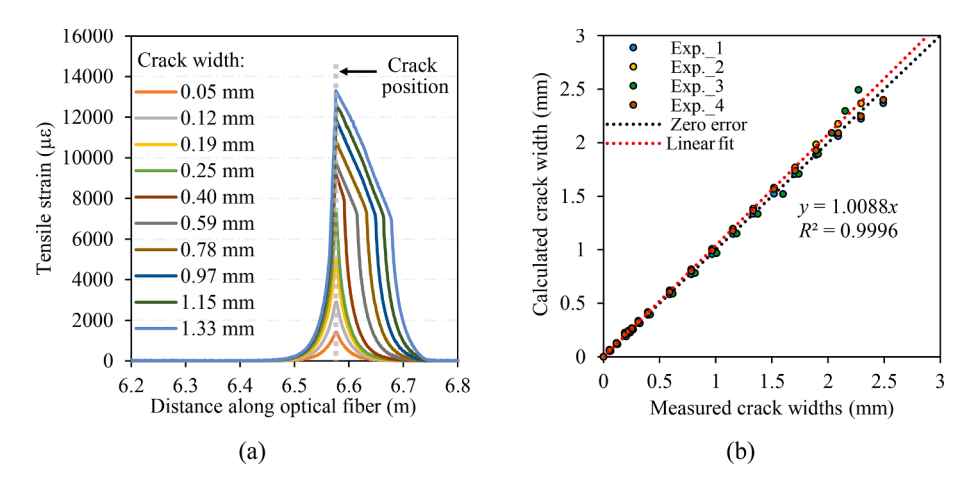


Fig. 16. Experimental results of unsymmetrical fiber pullout cases: (a) a typical unsymmetrical strain distribution result at different crack widths; and (b) measurement accuracy of the crack width.

$$w_c = w_L + w_R \tag{25a}$$

$$w_L = \int_0^{\ell_L} \varepsilon_f(x) dx \tag{25b}$$

$$w_R = \int_0^{\infty} \varepsilon_f(x) dx$$
 (25c)

$$\varepsilon_f(x = \ell_L) = \varepsilon_f(x = \ell_R)$$
 (25d)

Fig. 16(a) shows representative results of the unsymmetrical strain distributions measured from an optical fiber crossing a crack with the increase of the crack width. When the crack width is small (up to 0.25 mm), symmetrical strain distributions are observed, and there is no debonding. When the crack width is 0.40 mm or larger, debonding occurs at the right side, but does not occur at the left side. Fig. 16(b) compares the calculation and measurement results of crack widths. The crack widths were calculated by integrating the strain distributions in the distributed sensor at the two sides of the crack and measured using an extensometer. The calculation and measurement results of crack widths agree well with each other. A straight line can be used to fit the data, and the coefficient of determination (R^2) is 0.9996, which indicates a high correlation. The results corroborate that the proposed approach is applicable to unsymmetric cases.

5. Conclusions

This study presents a unified cohesive interface law to describe the bond-slip behavior of fused silica fiber with polymeric coating in the fiber pullout process, performs a mechanical analysis on fiber pullout responses based on the presented interface law, develops a metaheuristic inverse analysis to calibrate the model parameters, and applies a distributed fiber optic sensing technology based on

optical frequency domain reflectometry to measure the strain distributions in optical fibers. The developed method is applied to analyze the measurement from a distributed fiber optic sensor. The following findings are drawn:

- The presented CIL reasonably reflected the bond-slip behavior for fused silica fiber with polymeric coating and has the potential for other types of fiber—matrix interface. With the proposed CIL, the mechanical analysis on the fiber-coating interface can establish the intrinsic relationship between the CIL and the fiber pullout force-crack width response.
- The parameters of the unified CIL were automatically determined through the metaheuristic inverse analysis with high efficiency and accuracy. For the investigated embedment fiber lengths, the RMSE is lower than 0.13, R² is higher than 0.98, and MAE is lower than 0.11.
- The presented method provides reasonable predictions of the slip distribution and shear stress distribution at the fiber-coating interface as well as the strain distributions in the fused silica fiber. The results of the strain distributions agreed with the strain distributions measured from the distributed fiber optic sensors throughout the pullout process.
- This research establishes fundamental understanding of the fiber-coating interfacial behavior, and the understanding enables distributed fiber optic sensors to be operated in presence of debonding at the fiber-coating interface at crack, as well as accurate measurement of crack width opening by interpretation results obtained from distributed fiber optic sensors.

Declaration of Competing Interest

The authors declare that they have no known competing financial interests or personal relationships that could have appeared to influence the work reported in this paper.

Data availability

Data will be made available on request.

Acknowledgements

This research was funded by the United States Department of Transportation [grant number 693JK31950008CAAP] and National Science Foundation [grant number CMMI-2046407].

Appendix

Appendix A. . Derivation process of analytical solutions

A1. Case 1: Long embedment length $(\ell > \ell_0)$

With the CIL defined in Fig. 4, the governing equation was solved to determine the slip, shear stress, and axial strain distributions along the embedded fiber length, as well as the load-slip response of the fiber throughout the fiber pullout process, as elaborated in this section.

A1.1. Stage I: Elastic stage

Under small loads, the entire fiber–matrix interface remains elastic. When the shear stress at the loaded end of fiber reaches $\beta \tau_f$, in other words $s_G = \alpha s_f$, the elastic stage is ended. The bonded length is governed by the first stage of CIL, as expressed by Eq. (A.1):

$$\frac{d^2s(x)}{dx^2} - \lambda_1^2 s(x) = 0, 0 \le s \le \alpha s_f \tag{A.1}$$

$$\lambda_1 = \lambda \sqrt{\frac{\beta \tau_f}{\alpha s_f}}$$

By considering the boundary conditions in Eq. (6) and Eq. (7), the slip s(x), shear stress $\tau(x)$, and axial strain $\varepsilon(x)$ along the fiber are obtained as:

$$s(x) = s_F \cosh(\lambda_1 x)$$
 (A.2a)

$$\tau(x) = \frac{\beta \tau_f}{\alpha s_f} s_F \cosh(\lambda_1 x) \tag{A.2b}$$

$$\varepsilon_f(x) = \frac{1}{\omega} \lambda_1 s_F \sinh(\lambda_1 x)$$
 (A.2c)

Eq. (A.2a) is used to obtain the slip at the loaded end s_G :

$$s_G = s(\ell) = s_F \cosh(\lambda_1 \ell)$$
 (A.3)

By substituting Eq. (A.2c) into Eq. (7), the applied load P is obtained:

$$P = A_f E_f \frac{1}{\omega} \lambda_1 \sinh(\lambda_1 \ell) s_F = A_f E_f \lambda_1 \frac{1}{\omega} \tanh(\lambda_1 \ell) s_G \tag{A.4}$$

Eq. (A.4) indicates that *P* is proportional to s_G and s_F . The elastic stage is ended when $\tau(\ell) = \beta \tau_f$, in other words $s_G = \alpha s_f$, and the load at the end of the elastic stage is:

$$P_{A} = A_{f} E_{f} \lambda_{1} \frac{1}{\omega} \tanh(\lambda_{1} \angle) \alpha s_{f}$$
(A.5)

A1.2. Stage II: Elastic-yielding stage

As $s_G \ge \alpha s_f$, the second stage of the bond-slip curve commences at the loaded end, and the position of the shear stress $\beta \tau_f$ moves towards the free end of the fiber. When the shear stress at the loaded end reaches τ_f , in other words $s_G = s_f$, the elastic-yielding stage is ended, and the elastic-yielding-debonding stage is started. The entire bonded length is governed by the first and second stages of the CIL, expressed as:

$$\begin{cases} \frac{d^2 s(x)}{dx^2} - \lambda_1^2 s(x) = 0, 0 \le s \le \alpha s_f \\ \frac{d^2 s(x)}{dx^2} - \lambda_2^2 s(x) = \frac{\beta - \alpha}{1 - \beta} s_f \lambda_2^2, \alpha s_f \le s \le s_f \end{cases}$$
(A.6a)

(A.6b)

$$\text{where } \lambda_2 = \begin{cases} \lambda \sqrt{\frac{(1-\beta)\tau_f}{(1-\alpha)s_f}}, 0 < \beta < 1 \\ 0, \beta = 1 \\ \lambda \sqrt{\frac{(\beta-1)\tau_f}{(1-\alpha)s_f}}i, \beta > 1 \end{cases} \text{, and } i \text{ is the imaginary unit.}$$

Eq. (A.6) is solved using the boundary conditions:

$$s(0) = \frac{P}{\lambda_1 A_F E_F} \frac{1}{\sinh(\lambda_1 C)} = s_F \tag{A.7a}$$

$$\varepsilon_f^-(\ell_{el}) = \varepsilon_f^+(\ell_{el})$$
 (A.7b)

$$s^{-}(\ell_{el}) = s^{+}(\ell_{el}) = \alpha s_f \tag{A.7c}$$

where $\ell_{el} = \frac{1}{\lambda_1} \cosh^{-1} \left(\frac{as_f}{s_F} \right)$ is defined as the elastic length using the boundary conditions. The yielding length is defined as $\ell_{yd} = \ell_{el}$.

The solution at the region of $0 \le x \le \ell_{el}$ is expressed as:

$$s(x) = \alpha s_f \frac{\cosh(\lambda_1 x)}{\cosh(\lambda_1 \ell_{ef})}$$
(A.8a)

$$\tau(x) = \beta \tau_f \frac{\cosh(\lambda_1 x)}{\cosh(\lambda_1 \ell_{eff})} \tag{A.8b}$$

$$\varepsilon_f(x) = \frac{1}{\varphi} \lambda_1 \alpha s_f \frac{\sinh(\lambda_1 x)}{\cosh(\lambda_1 \ell_{ef})} \tag{A.8c}$$

The solution at the region of $\ell_{el} \le x \le \ell$ is expressed as:

$$s(x) = \begin{cases} \frac{(1-\alpha)\beta s_f}{1-\beta} \cosh[\lambda_2(\ell_{el}-x)] - \frac{\lambda_1 \alpha s_f}{\lambda_2} \tanh(\lambda_1 \ell_{el}) \sinh[\lambda_2(\ell_{el}-x)] - \frac{\beta-\alpha}{1-\beta} s_f, \beta \neq 1 \\ \frac{1}{2} \lambda^2 \tau_f(\ell_{el}-x)^2 - \lambda_1 \alpha_f \tanh(\lambda_1 \ell_{el}) \bullet (\ell_{el}-x) + \alpha s_f, \beta = 1 \end{cases}$$
(A.9a)

$$\tau(x) = \begin{cases} \beta \tau_f \cosh[\lambda_2(\ell_{el} - x)] - \frac{\alpha(1 - \beta)\lambda_1 \tau_f}{(1 - \alpha)\lambda_2} \tanh(\lambda_1 \ell_{el}) \sinh[\lambda_2(\ell_{el} - x)], \beta \neq 1 \\ \tau_f, \beta = 1 \end{cases}$$
(A.9b)

$$\varepsilon_{f}(x) = \begin{cases} \frac{1}{\varphi} \lambda_{1} \alpha s_{f} \tanh(\lambda_{1} \ell_{el}) \cosh[\lambda_{2} (\ell_{el} - x)] - \frac{1}{\varphi} \lambda_{2} \frac{(1 - \alpha)\beta s_{f}}{1 - \beta} \sinh[\lambda_{2} (\ell_{el} - x)], \beta \neq 1 \\ -\frac{1}{\varphi} \lambda^{2} \tau_{f} (\ell_{el} - x) + \frac{1}{\varphi} \lambda_{1} \alpha_{f} \tanh(\lambda_{1} \ell_{el}), \beta = 1 \end{cases}$$
(A.9c)

Eq. (A.9a) can be used to obtain s_G by letting $x = \ell$:

$$s_{G} = \begin{cases} \frac{(1-\alpha)\beta s_{f}}{1-\beta} \cosh[\lambda_{2}(\ell_{el}-\ell)] - \frac{\lambda_{1}\alpha s_{f}}{\lambda_{2}} \tanh(\lambda_{1}\ell_{el}) \sinh[\lambda_{2}(\ell_{el}-\ell)] - \frac{\beta-\alpha}{1-\beta} s_{f}, \beta \neq 1\\ \frac{1}{2}\lambda^{2} \tau_{f}(\ell_{el}-\ell)^{2} - \lambda_{1}\alpha_{f} \tanh(\lambda_{1}\ell_{el}) \bullet (\ell_{el}-\ell) + \alpha s_{f}, \beta = 1 \end{cases}$$
(A.10)

By substituting Eq. (A.9c) into Eq. (7), the applied load P is obtained:

$$P = \begin{cases} A_{f} E_{f} \left[\frac{1}{\varphi} \lambda_{1} \alpha s_{f} \tanh(\lambda_{1} \ell_{el}) \cosh[\lambda_{2} (\ell_{el} - \ell')] - \frac{1}{\varphi} \lambda_{2} \frac{(1 - \alpha) \beta s_{f}}{1 - \beta} \sinh[\lambda_{2} (\ell_{el} - \ell')] \right], \beta \neq 1 \\ A_{f} E_{f} \left[-\frac{1}{\varphi} \lambda^{2} \tau_{f} (\ell_{el} - \ell') + \frac{1}{\varphi} \lambda_{1} \alpha_{f} \tanh(\lambda_{1} \ell_{el}) \right], \beta = 1 \end{cases}$$
(A.11)

When $s_G = s_f$, the shear stress at the loaded end reaches τ_f , so substituting $\tau(x) = \tau_f$ into Eq.(A.9b) leads to:

$$\frac{(1-\alpha)\lambda_2}{\alpha(1-\beta)\lambda_1} \left[\frac{1-\beta \cosh\left(\lambda_2 \ell_{yd}\right)}{\sinh\left(\lambda_2 \ell_{yd}\right)} \right] = \tanh(\lambda_1 \ell_{el}) \tag{A.12}$$

Eq.(A.12) can be interactively solved to compute the value yielding length at the debonding load ($\ell_{yd,C}$) when considering:

$$\ell_{yd} = \ell - \ell_{el} \tag{A.13}$$

Then the elastic length at the debonding load ($V_{el,C}$) and the corresponding value of free end slip ($s_{F,C}$) can be determined. Finally, the debonding load P_{deb} is expressed as:

$$P_{C} = \begin{cases} A_{f}E_{f} \left[\frac{1}{\varphi} \lambda_{1} \alpha s_{f} \tanh\left(\lambda_{1} \ell_{el,C}\right) \cosh\left(\lambda_{2} \ell_{yd,C}\right) + \frac{1}{\varphi} \lambda_{2} \frac{(1-\alpha)\beta s_{f}}{1-\beta} \sinh\left(\lambda_{2} \ell_{yd,C}\right) \right], \beta \neq 1 \\ A_{f}E_{f} \left[\frac{1}{\varphi} \lambda^{2} \tau_{f} \left(\ell_{yd,C}\right) + \frac{1}{\varphi} \lambda_{1} \alpha_{f} \tanh\left(\lambda_{1} \ell_{el,C}\right) \right], \beta = 1 \end{cases}$$

$$(A.14)$$

A1.3. Stage III: Elastic-yielding-debonding stage

As $s_G \ge s_f$, the elastic-yielding-debonding stage is started. The interface has a combination of elastic, yielding, and debonding regions. When the free end slip s_F reaches αs_f at x=0 ($s_F=\alpha s_f$), the elastic-yielding-debonding stage is ended. The governing equations are expressed as:

$$\begin{cases} \frac{d^2 s(x)}{dx^2} - \lambda_1^2 s(x) = 0, 0 \le s \le \alpha s_f \\ \frac{d^2 s(x)}{dx^2} - \lambda_2^2 s(x) = \frac{\beta - \alpha}{1 - \beta} s_f \lambda_2^2, \alpha s_f \le s \le s_f \\ \frac{d^2 s(x)}{dx^2} - \lambda_3^2 \frac{2k}{\tau_f} e^{\frac{-\tau_f}{k} s(x)} = 0, s > s_f \end{cases}$$
(A.15)

$$\lambda_3 = \lambda \sqrt{e^{\frac{\tau_f s_f}{k}} \bullet \frac{{\tau_f}^2}{2k}}$$

Eq. (A.15) can be solved using the boundary conditions:

$$s(0) = s_F = \frac{P}{\lambda_1 A_f E_f} \frac{1}{\sinh(\lambda_1 \ell)}$$
(A.16a)

$$\varepsilon_f^-(\ell_{el}) = \varepsilon_f^+(\ell_{el})$$
 (A.16b)

$$s^{-}(\ell_{el}) = s^{+}(\ell_{el}) = \alpha s_{f}$$
 (A.16c)

$$\varepsilon_f^-(\ell_{el} + \ell_{vd}) = \varepsilon_f^+(\ell_{el} + \ell_{vd}) \tag{A.16d}$$

$$s^{-}(\ell_{el} + \ell_{vd}) = s^{+}(\ell_{el} + \ell_{vd}) = s_f \tag{A.16e}$$

where ℓ_{el} and ℓ_{yd} are the elastic length and the yielding length, respectively, which are determined by the boundary conditions. The solution of Eq. (A.15a) is the same as Eq. (A.8a).

In addition, based on Eqs. (A.16c) and (A.16e), the solution of Eq. (A.15b) is expressed as:

$$s(x) = \begin{cases} \frac{(1-\alpha)\beta s_f}{1-\beta} \frac{\sinh\left[\lambda_2(\ell_{el}+\ell_{yd}-x)\right]}{\sinh\left(\lambda_2\ell_{yd}\right)} - \frac{(1-\alpha)s_f}{1-\beta} \frac{\sinh\left[\lambda_2(\ell_{el}-x)\right]}{\sinh\left(\lambda_2\ell_{yd}\right)} - \frac{\beta-\alpha}{1-\beta}s_f, \beta \neq 1\\ \frac{1}{2}\lambda^2 \tau_f(\ell_{el}-x)(\ell_{el}+\ell_{yd}-x) - \frac{(1-\alpha)s_f}{\ell_{yd}}(\ell_{el}-x) + \alpha s_f, \beta = 1 \end{cases}$$
(A.17a)

$$\tau(x) = \begin{cases} \beta \tau_f \frac{\sinh\left[\lambda_2 \left(\ell_{el} + \ell_{yd} - x\right)\right]}{\sinh\left(\lambda_2 \ell_{yd}\right)} - \tau_f \frac{\sinh\left[\lambda_2 \left(\ell_{el} - x\right)\right]}{\sinh\left(\lambda_2 \ell_{yd}\right)}, \beta \neq 1\\ \tau_f, \beta = 1 \end{cases}$$
(A.17b)

$$\varepsilon_{f}(x) = \begin{cases} -\frac{1}{\varphi} \lambda_{2} \frac{(1-\alpha)\beta s_{f}}{1-\beta} \frac{\cosh\left[\lambda_{2}\left(\ell_{el} + \ell_{yd} - x\right)\right]}{\sinh\left(\lambda_{2}\ell_{yd}\right)} + \frac{1}{\varphi} \lambda_{2} \frac{(1-\alpha)s_{f}}{1-\beta} \frac{\cosh\left[\lambda_{2}\left(\ell_{el} - x\right)\right]}{\sinh\left(\lambda_{2}\ell_{yd}\right)}, \beta \neq 1 \\ -\frac{1}{\varphi} \lambda^{2} \tau_{f}(\ell_{el} - x) - \frac{1}{2} \frac{1}{\varphi} \lambda^{2} \tau_{f}\ell_{yd} + \frac{1}{\varphi} \frac{(1-\alpha)s_{f}}{\ell_{yd}}, \beta = 1 \end{cases}$$
(A.17c)

Based on the reducing order approach [24], the solution of Eq. (A.15c) is expressed as:

$$s(x) = \frac{2k}{\tau_f} \ln \left\{ \cosh \left[\lambda_3 \sqrt{C_1} \left(x - C_2 \right) \right] \right\} - \frac{k}{\tau_f} \ln(C_1)$$
(A.18a)

$$\tau(x) = \frac{C_1 \tau_f \bullet e^{\frac{\tau_f f_f}{k}}}{\cosh^2 \left[\lambda_3 \sqrt{C_1} \left(x - C_2 \right) \right]} \tag{A.18b}$$

$$\varepsilon_f(x) = \frac{1}{\alpha} \frac{2k}{\tau_c} \lambda_3 \sqrt{C_1} \tanh \left[\lambda_3 \sqrt{C_1} \left(x - C_2 \right) \right]$$
(A.18c)

where constants C_1 and C_2 are determined by Eqs. (A.16d) and (A.16e):

$$C_{1} = \begin{cases} \left[\frac{\tau_{f} s_{f} \lambda_{2} (1 - \alpha)}{2k \lambda_{3} (1 - \beta)} \frac{\left(\cosh\left(\lambda_{2} \ell_{yd}\right) - \beta\right)}{\sinh\left(\lambda_{2} \ell_{yd}\right)} \right]^{2} + e^{-\left(\frac{\tau_{f} s_{f}}{k}\right)}, \beta \neq 1 \\ \left[\frac{\frac{1}{2} \lambda^{2} \tau_{f}^{2} \ell_{yd} + \frac{(1 - \alpha) s_{f} \tau_{f}}{\ell_{yd}}}{2k \lambda_{3}} \right]^{2} + e^{-\left(\frac{\tau_{f} s_{f}}{k}\right)}, \beta = 1 \end{cases}$$

$$(A.19a)$$

$$C_{2} = \begin{cases} \ell_{el} + \ell_{yd} - \frac{1}{\lambda_{3}\sqrt{C_{1}}} \tanh^{-1} \left[\frac{\tau_{f} s_{f} \lambda_{2} (1 - \alpha)}{2k\sqrt{C_{1}} \lambda_{3} (1 - \beta)} \frac{\left(\cosh\left(\lambda_{2} \ell_{yd}\right) - \beta\right)}{\sinh\left(\lambda_{2} \ell_{yd}\right)} \right], \beta \neq 1 \\ \ell_{el} + \ell_{yd} - \frac{1}{\lambda_{3}\sqrt{C_{1}}} \tanh^{-1} \left[\frac{1}{2} \lambda^{2} \tau_{f}^{2} \ell_{yd} + \frac{(1 - \alpha)s_{f} \tau_{f}}{\ell_{yd}}}{2k\sqrt{C_{1}} \lambda_{3}} \right], \beta = 1 \end{cases}$$

$$(A.19b)$$

Substituting Eq. (7) into Eq. (A.18c), the following equation is obtained:

$$P = A_f E_f \frac{1}{\omega} \frac{2k}{\tau_c} \lambda_3 \sqrt{C_1} \tanh \left[\lambda_3 \sqrt{C_1} \left(\ell - C_2 \right) \right]$$
(A.20)

When $x = \ell$, the expression of the slip at the loaded end is obtained from Eq. (A.18a):

$$s_G = \frac{2k}{\tau_f} \ln \left\{ \cosh \left[\lambda_3 \sqrt{C_1} \left(\ell - C_2 \right) \right] \right\} - \frac{k}{\tau_f} \ln(C_1)$$
(A.21)

According to Eq. (A.16b), the relational expression between the yielding length ℓ_{vd} and the elastic length ℓ_{el} is obtained:

$$\begin{cases}
\frac{\lambda_{2}(1-\alpha)}{1-\beta} \frac{\left[1-\beta \cosh\left(\lambda_{2} \ell_{yd}\right)\right]}{\sinh\left(\lambda_{2} \ell_{yd}\right)} = \lambda_{1} \alpha \tanh\left(\lambda_{1} \ell_{el}\right), \beta \neq 1 \\
-\frac{1}{2} \lambda^{2} \tau_{f} \ell_{yd} + \frac{(1-\alpha)s_{f}}{\ell_{yd}} = \lambda_{1} \alpha \tanh\left(\lambda_{1} \ell_{el}\right), \beta = 1
\end{cases}$$
(A.22)

Considering $\ell_{el} = \frac{1}{l_1} \cosh^{-1} \left(\frac{as_f}{s_F} \right)$, the general solution of ℓ_{yd} is given as:

$$\ell_{yd} = \begin{cases}
\frac{1}{\lambda_{2}} cosh^{-1} \begin{cases}
\frac{1}{\beta} + \sqrt{\left(\frac{\lambda_{1}\alpha(1-\alpha)}{\lambda_{2}\beta(1-\beta)}\right)^{2} \left(1 - \left(\frac{s_{F}}{\alpha s_{f}}\right)^{2}\right)} \sqrt{\left(\frac{\lambda_{1}\alpha(1-\alpha)}{\lambda_{2}\beta(1-\beta)}\right)^{2} \left(1 - \left(\frac{s_{F}}{\alpha s_{f}}\right)^{2}\right) + \left(1 - \frac{1}{\beta^{2}}\right)} \\
1 + \left(\frac{\lambda_{1}\alpha(1-\alpha)}{\lambda_{2}\beta(1-\beta)}\right)^{2} \left(1 - \left(\frac{s_{F}}{\alpha s_{f}}\right)^{2}\right) \\
-\frac{\lambda_{1}\alpha}{\lambda^{2}\tau_{f}} \sqrt{1 - \left(\frac{s_{F}}{\alpha s_{f}}\right)^{2}} + \sqrt{\left(\frac{\lambda_{1}\alpha}{\lambda^{2}\tau_{f}}\right)^{2} \left(1 - \left(\frac{s_{F}}{\alpha s_{f}}\right)^{2}\right) + \frac{2(1-\alpha)s_{f}}{\lambda^{2}\tau_{f}}}, \beta = 1
\end{cases}$$
(A.23a)

This stage is ended when $\ell_{el}=0$. Then, the following relationship is obtained:

$$\ell_{yd,max} = \begin{cases}
\frac{1}{\lambda_2} \cosh^{-1}\left(\frac{1}{\beta}\right), \beta \neq 1 \\
\frac{1}{\lambda} \sqrt{\frac{2(1-\alpha)s_f}{\tau_f}}, \beta = 1
\end{cases}$$
(A.23b)

Given Eq. (A.23), it is found that $\ell_{yd,max} = \ell_0$. The elastic, yielding, and debonding stages can occur at the fiber-coating interface simultaneously only when ℓ is longer than ℓ_0 .

A1.4. Stage IV: Yielding-debonding stage

When $s_F \ge \alpha s_f$, the elastic region ended at the free end of the fiber, and the shear stress decreases from τ_f to zero along the debonding length (ℓ_{db}). When the shear stress at the free end is τ_f ($s_F = s_f$), the yielding-debonding stage is ended, and the debonding stage starts. The entire interface enters the debonding stage at the end of the yielding-debonding stage when $\ell_{db} = \ell$.

The entire bonded length is governed by the second and third stages of CIL, as expressed by Eq. (A.24):

$$\begin{cases} \frac{d^2 s(x)}{dx^2} - \lambda_2^2 s(x) = \frac{\beta - \alpha}{1 - \beta} s_f \lambda_2^2, \alpha s_f \le s < s_f \\ \frac{d^2 s(x)}{dx^2} - \lambda_3^2 \frac{2k}{\tau_f} e^{\frac{-\tau_f}{k} s(x)} = 0, s \ge s_f \end{cases}$$
(A.24)

Eq. (A.24) is solved by the boundary conditions:

$$s(0) = s_F = \begin{cases} \frac{P}{\lambda_2 A_f E_f} \frac{1}{\sinh(\lambda_2 \ell)} - \frac{\beta - \alpha}{1 - \beta} s_f, \beta \neq 1 \\ s_F, \beta = 1 \end{cases}$$
(A.25a)

$$\varepsilon_f^-(\ell_{vd}) = \varepsilon_f^+(\ell_{vd})$$
 (A.25b)

$$s^{-}(\ell_{yd}) = s^{+}(\ell_{yd}) = s_f \tag{A.25c}$$

$$\text{where } \mathscr{N}_{yd} = \begin{cases} \frac{1}{\lambda_2} \cosh^{-1} \left(\frac{s_f + \frac{\beta - \alpha}{1 - \beta} s_f}{s_F + \frac{\beta - \alpha}{1 - \beta} s_f} \right), \beta \neq 1 \\ \frac{1}{\lambda} \sqrt{\frac{2(s_F - s_f)}{\tau_f}}, \beta = 1 \end{cases}, \text{ to be determined using Eqs. (A.25b) and (A.25c)}.$$

The solutions of the Eq. (A.24a) are expressed as:

$$s(x) = \begin{cases} \frac{1-\alpha}{1-\beta} s_f \frac{\cosh(\lambda_2 x)}{\cosh(\lambda_2 \ell_{yd})} - \frac{\beta-\alpha}{1-\beta} s_f, \beta \neq 1\\ \frac{1}{2} \lambda^2 \tau_f (x^2 - \ell_{yd}^2) + s_f, \beta = 1 \end{cases}$$
(A.26a)

$$\tau(x) = \begin{cases} \tau_f \frac{\cosh(\lambda_2 x)}{\cosh(\lambda_2 \ell_{yd})}, \beta \neq 1\\ \tau_f, \beta = 1 \end{cases}$$
(A.26b)

$$\varepsilon_f(x) = \begin{cases} \frac{1}{\varphi} \lambda_2 \frac{1 - \alpha}{1 - \beta} s_f \frac{\sinh(\lambda_2 x)}{\cosh(\lambda_2 \ell_{yd})}, \beta \neq 1\\ \frac{1}{\varphi} \lambda_2^2 \tau_f x, \beta = 1 \end{cases}$$
(A.26c)

The solutions of the Eq. (A.24b) are expressed as:

$$s(x) = \frac{2k}{\tau_f} \ln \left\{ \cosh \left[\lambda_3 \sqrt{C_3} \left(x - C_4 \right) \right] \right\} - \frac{k}{\tau_f} \ln(C_3)$$
(A.27a)

$$\tau(x) = \frac{C_3 \tau_f \bullet e^{\frac{\tau_f \tau_f}{k}}}{\cosh^2 \left[\lambda_3 \sqrt{C_3} \left(x - C_4 \right) \right]} \tag{A.27b}$$

$$\varepsilon_f(x) = \frac{1}{\varphi} \frac{2k}{\tau_f} \lambda_3 \sqrt{C_3} \tanh \left[\lambda_3 \sqrt{C_3} \left(x - C_4 \right) \right] \tag{A.27c}$$

The constants, C_3 and C_4 , are determined as:

$$C_{3} = \begin{cases} \left[\frac{\tau_{f}s_{f}\lambda_{2}(1-\alpha)}{2k\lambda_{3}(1-\beta)}\tanh(\lambda_{2}\ell_{yd})\right]^{2} + e^{-\left(\frac{\tau_{f}s_{f}}{k}\right)}, \beta \neq 1\\ \left[\frac{\lambda^{2}\tau_{f}^{2}\ell_{yd}}{2k\lambda_{3}}\right]^{2} + e^{-\left(\frac{\tau_{f}s_{f}}{k}\right)}, \beta = 1 \end{cases}$$
(A.28a)

$$C_{4} = \begin{cases} \mathcal{N}_{yd} - \frac{1}{\lambda_{3}\sqrt{C_{3}}} \tanh^{-1} \left[\frac{\tau_{f} s_{f} \lambda_{2} (1 - \alpha)}{2k\sqrt{C_{3}} \lambda_{3} (1 - \beta)} \tanh \left(\lambda_{2} \mathcal{N}_{yd} \right) \right], \beta \neq 1 \\ \\ \mathcal{N}_{yd} - \frac{1}{\lambda_{3}\sqrt{C_{3}}} \tanh^{-1} \left[\frac{\lambda^{2} \tau_{f}^{2} \mathcal{N}_{yd}}{2k\sqrt{C_{3}} \lambda_{3}} \right], \beta = 1 \end{cases}$$

$$(A.28b)$$

Eq. (A.27a) is used to obtain the slip at the loaded end:

$$s_G = s(\ell) = \frac{2k}{\tau_f} \ln\left\{\cosh\left[\lambda_3 \sqrt{C_3} \left(\ell - C_4\right)\right]\right\} - \frac{k}{\tau_f} \ln(C_3) \tag{A.29}$$

By substituting Eq. (A.27c) into Eq. (7), the applied load P is obtained as:

$$P = A_f E_f \frac{1}{\varphi} \frac{2k}{\tau_f} \lambda_3 \sqrt{C_3} \tanh \left[\lambda_3 \sqrt{C_3} \left(\ell - C_4 \right) \right]$$
(A.30)

$$P_{E} = A_{f} E_{f} \frac{2k}{\varphi} \lambda_{3} e^{-\left(\frac{r_{f} s_{f}}{2k}\right)} \tanh\left(\lambda_{3} e^{-\left(\frac{r_{f} s_{f}}{2k}\right)}\ell\right) \tag{A.31}$$

The yielding-debonding stage is ended when the entire length of the interface enters the debonding stage ($s_{F.E} = s_f$), and the corresponding load P_E is expressed as:

The corresponding global slip s_{GE} is expressed as:

$$s_{G,E} = \frac{2k}{\tau_f} \ln \left[\cosh \left(\lambda_3 e^{-\left(\frac{\tau_f s_f}{2k} \right)} \right) \right] + s_f \tag{A.32}$$

A1.5. Stage V: Debonding stage

The debonding stage starts when $\ell_{db} = \ell$. In the debonding stage, the bonded length ℓ_{db} decreases from ℓ to zero. Then, the load-carry capacity is provided by the interface friction.

The entire bonded length is governed by the third stage of CIL, as expressed by Eq. (A.33):

$$\frac{d^2s(x)}{dx^2} - \lambda_3^2 \frac{2k}{\tau_f} e^{\frac{-\tau_f}{k}s(x)} = 0, s_f \le s_F$$
(A.33)

The slip s(x), shear stress $\tau(x)$, and axial strain $\varepsilon(x)$ in the debonding region are expressed as:

$$s(x) = \frac{2k}{\tau_f} \ln \left\{ \cosh \left[\lambda_3 \sqrt{C_5} \left(x - C_6 \right) \right] \right\} - \frac{k}{\tau_f} \ln(C_5)$$
(A.34a)

$$\tau(x) = \frac{C_5 \tau_f \bullet e^{\frac{\tau_f \tau_f}{k}}}{\cosh^2 \left[\lambda_3 \sqrt{C_5} \left(x - C_6 \right) \right]} \tag{A.34b}$$

$$\varepsilon_f(x) = \frac{1}{\varphi} \frac{2k}{\tau_f} \lambda_3 \sqrt{C_5} \tanh \left[\lambda_3 \sqrt{C_5} \left(x - C_6 \right) \right] \tag{A.34c}$$

The constants C_5 and C_6 are determined as:

$$C_5 = e^{-\left(\frac{r_f r_F}{k}\right)} \tag{A.35a}$$

$$C_6 = 0 (A.35b)$$

Eq. (A.34a) is used to obtain the slip at the loaded end:

$$s_G = s(\ell) = \frac{2k}{\tau_F} \ln \left[\cosh \left(\lambda_3 e^{-\left(\frac{\tau_f s_F}{2k} \right)} \ell \right) \right] + s_F \tag{A.36}$$

By substituting Eq. (A.34c) into Eq. (7), the applied load P is obtained as:

$$P = A_f E_f \frac{1}{\varphi} \frac{2k}{\tau_f} \lambda_3 e^{-\left(\frac{\tau_f s_F}{2k}\right)} \tanh\left(\lambda_3 e^{-\left(\frac{\tau_f s_F}{2k}\right)} \ell\right) \tag{A.37}$$

A2. Case 2: Short embedment length ($\ell < \ell_0$)

When the embedment length of fiber is shorter than the critical embedment length ($\ell < \ell_0$), the elastic-yielding-debonding stage in Case 1 is replaced by a yielding stage. The other stages in Cases 1 and Case 2 are the same, so they are not duplicated. This section only elaborates the yielding stage.

When $s_F \ge \alpha s_f$, stage III starts, and the entire bonded length enters the yielding stage. The shear stress along the entire embedment length is within the yielding stage ($\ell_{yd} = \ell$). When the shear stress at the loaded end of the fiber reaches τ_f , in other words $s_G = s_f$, the yielding stage is ended and the yielding-debonding stage is started. The entire bonded length is governed by the second stage of CIL, as expressed by Eq. (A.38):

$$\frac{d^2s(x)}{dx^2} - \lambda_2^2 s(x) = \frac{\beta - \alpha}{1 - \beta} s_f \lambda_2^2, \alpha s_f \le s \le s_f$$
(A.38)

where $\ell = \ell_{yd}$ in the yielding stage.

The solutions of slip s(x), shear stress $\tau(x)$, and axial strain $\varepsilon(x)$ in the yielding stage are:

$$s(x) = \begin{cases} \left(s_F + \frac{\beta - \alpha}{1 - \beta}s_f\right) \cosh(\lambda_2 x) - \frac{\beta - \alpha}{1 - \beta}s_f, \beta \neq 1\\ \frac{1}{2}\lambda^2 \tau_f x^2 + s_F, \beta = 1 \end{cases}$$
(A.39a)

$$\tau(x) = \begin{cases} \left[\frac{(1-\beta)\tau_f}{(1-\alpha)s_f} s_F + \frac{\beta-\alpha}{1-\alpha} \tau_f \right] \cosh(\lambda_2 x), \beta \neq 1 \\ \tau_f, \beta = 1 \end{cases}$$
(A.39b)

$$\varepsilon_f(x) = \begin{cases} \frac{1}{\varphi} \lambda_2 \left(s_F + \frac{\beta - \alpha}{1 - \beta} s_f \right) \sinh(\lambda_2 x), \beta \neq 1 \\ \frac{1}{\varphi} \lambda^2 \tau_f x, \beta = 1 \end{cases}$$
(A.39c)

Eq. (A.39a) is used to determine the slips at the free end and loaded end, respectively:

$$s_F = \begin{cases} \frac{P}{\lambda_2 A_f E_f} \frac{1}{\sinh(\lambda_2 \mathscr{N})} - \frac{\beta - \alpha}{1 - \beta} s_f, \beta \neq 1 \\ s_F, \beta = 1 \end{cases}$$
(A.40)

$$s_{G} = \begin{cases} \frac{P}{\lambda_{2} A_{f} E_{f}} \frac{1}{\tanh(\lambda_{2} \ell)} - \frac{\beta - \alpha}{1 - \beta} s_{f}, \beta \neq 1 \\ \frac{P}{2 A_{f} E_{f}} l + s_{F}, \beta = 1 \end{cases}$$
(A.41)

Stage III is ended when $s_{G,D} = s_f$. The corresponding load is P_D :

$$P_{D} = \begin{cases} A_{f}E_{f}\frac{1}{\varphi}\left(\frac{1-\alpha}{1-\beta}\right)s_{f}\lambda_{2}\tanh(\lambda_{2}\mathscr{L}), \beta \neq 1\\ A_{f}E_{f}\frac{1}{\varphi}\lambda^{2}\tau_{f}l, \beta = 1 \end{cases}$$
(A.42)

References

- [1] M. Li, X. Feng, Y. Han, Brillouin fiber optic sensors and mobile augmented reality-based digital twins for quantitative safety assessment of underground pipelines, Autom. Constr. 144 (2022), 104617, https://doi.org/10.1016/j.autcon.2022.104617.
- [2] S. Zhang, H. Liu, J. Cheng, M.J. DeJong, A mechanical model to interpret distributed fiber optic strain measurement at displacement discontinuities. Structural Health Monitoring, Struct. Health Monit. 20 (5) (2021) 2584–2603.
- [3] J.M. Henault, M. Quiertant, S. Delepine-Lesoille, J. Salin, G. Moreau, F. Taillade, K. Benzarti, Quantitative strain measurement and crack detection in RC structures using a truly distributed fiber optic sensing system, Constr. Build. Mater. 37 (2012) 916–923, https://doi.org/10.1016/j.conbuildmat.2012.05.029.
- [4] L. Fan, Y. Bao, Review of fiber optic sensors for corrosion monitoring in reinforced concrete, Cem. Concr. Compos. 120 (2021), 104029, https://doi.org/10.1016/j.cemconcomp.2021.104029.
- [5] Y. Yao, M. Yan, Y. Bao, Measurement of cable forces for automated monitoring of engineering structures using fiber optic sensors: A review, Autom. Constr. 126 (2021), 103687, https://doi.org/10.1016/j.autcon.2021.103687.
- [6] B.K. Oh, H.S. Park, B. Glisic, Prediction of long-term strain in concrete structure using convolutional neural networks, air temperature and time stamp of measurements, Autom. Constr. 126 (2021), 103665, https://doi.org/10.1016/j.autcon.2021.103665.
- [7] D. Meng, F. Ansari, X. Feng, Detection and monitoring of surface micro-cracks by PPP-BOTDA, Appl. Opt. 54 (16) (2015) 4972–4978, https://doi.org/10.1364/A0.54.004972.
- [8] X. Tan, Y. Bao, Q. Zhang, H. Nassif, G. Chen, Strain transfer effect in distributed fiber optic sensors under an arbitrary field, Autom. Constr. 124 (2021), 103597, https://doi.org/10.1016/j.autcon.2021.103597.
- [9] S. Mahjoubi, X. Tan, Y. Bao, Inverse analysis of strain distributions sensed by distributed fiber optic sensors subject to strain transfer, Mech. Syst. Sig. Process. 166 (2022), 108474, https://doi.org/10.1016/j.ymssp.2021.108474.
- 166 (2022), 1084/4, https://doi.org/10.1016/j.ymssp.2021.1084/4. [10] M. Yan, X. Tan, S. Mahjoubi, Y. Bao, Strain transfer effect on measurements with distributed fiber optic sensors, Autom. Constr. 139 (2022), 104262, https://doi.
- org/10.1016/j.autcon.2022.104262.
 [11] X. Tan, Y. Bao, Measuring crack width using a distributed fiber optic sensor based on optical frequency domain reflectometry, Measurement 172 (2021),
- 108945, https://doi.org/10.1016/j.measurement.2020.108945.
 [12] X. Tan, A. Abu-Obeidah, Y. Bao, H. Nassif, W. Nasreddine, Measurement and visualization of strains and cracks in CFRP post-tensioned fiber reinforced concrete
- beams using distributed fiber optic sensors, Autom. Constr. 124 (2021), 103604, https://doi.org/10.1016/j.autcon.2021.103604.
 [13] H. Li, G. Zhou, L. Ren, D. Li, Strain transfer coefficient analyses for embedded fiber Bragg grating sensors in different host materials, J. Eng. Mech. 135 (12)
- (2009) 1343–1353, https://doi.org/10.1061/(ASCE)0733-9399(2009)135:12(1343).
 [14] A. Bassil, X. Wang, X. Chapeleau, E. Niederleithinger, O. Abraham, D. Leduc, Distributed fiber optics sensing and coda wave interferometry techniques for
- damage monitoring in concrete structures, Sensors 19 (2) (2019) 356, https://doi.org/10.3390/s19020356.
 [15] Y. Bao, M. Valipour, W. Meng, K.H. Khayat, G. Chen, Distributed fiber optic sensor-enhanced detection and prediction of shrinkage-induced delamination of
- ultra-high-performance concrete overlay, Smart Mater. Struct. 26 (8) (2017), 085009, https://doi.org/10.1088/1361-665X/aa71f4.
 [16] X. Feng, J. Zhou, C. Sun, X. Zhang, F. Ansari, Theoretical and experimental investigations into crack detection with BOTDR-distributed fiber optic sensors,
- J. Eng. Mech. 139 (12) (2013) 1797–1807, https://doi.org/10.1061/(ASCE)EM.1943-7889.0000622.
 [17] A.S. Calabrese, P. Colombi, T. D'Antino, Analytical solution of the bond behavior of FRCM composites using a rigid-softening cohesive material law, Compos. B
- Eng. 174 (2019), 107051, https://doi.org/10.1016/j.compositesb.2019.107051.
 [18] X. Zou, L.H. Sneed, T. D'Antino, Full-range behavior of fiber reinforced cementitious matrix (FRCM)-concrete joints using a trilinear bond-slip relationship, Compos. Struct. 239 (2020), 112024, https://doi.org/10.1016/j.compstruct.2020.112024.
- [19] T.R.E. Simpson, J.L. Keddie, Evidence from information of the control of the
- sensitive adhesive laminates, J. Adhes. 79 (12) (2003) 1207–1218, https://doi.org/10.1080/714906164.
 [20] H. Park, S.H. Lee, Review on interfacial bonding mechanism of functional polymer coating on glass in atomistic modeling perspective, Polymers 13 (14) (2021) 2244, https://doi.org/10.3390/polym13142244.
- [21] Z. Chen, W. Yan, A shear-lag model with a cohesive fibre–matrix interface for analysis of fibre pull-out, Mech. Mater. 91 (2015) 119–135, https://doi.org/10.1016/j.mechmat.2015.07.007.

- [22] Q. Meng, M. Chang, Interfacial crack propagation between a rigid fiber and a hyperelastic elastomer: Experiments and modeling, Int. J. Solids Struct. 188 (2020) 141–154, https://doi.org/10.1016/j.ijsolstr.2019.10.006.
- [23] Ö. Türkmen, S.N. Wijte, J. Vaculik, B. De Vries, J. Ingham, High-speed pullout behavior of deep-mounted CFRP strips bonded with a flexible adhesive to clay brick masonry, Structures 28 (2020) 1153–1172, https://doi.org/10.1016/j.istruc.2020.09.026.
- [24] H. Yuan, X. Lu, D. Hui, L. Feo, Studies on FRP-concrete interface with hardening and softening bond-slip law, Compos. Struct. 94 (12) (2012) 3781–3792, https://doi.org/10.1016/j.compstruct.2012.06.009.
- [25] E. Cosenza, G. Manfredi, R. Realfonzo, Behavior and modeling of bond of FRP rebars to concrete, J. Compos. Constr. 1 (2) (1997) 40–51, https://doi.org/10.1061/(ASCE)1090-0268(1997)1:2(40).
- [26] A. Caggiano, E. Martinelli, A unified formulation for simulating the bond behaviour of fibres in cementitious materials, Mater. Des. 42 (2012) 204–213, https://doi.org/10.1016/j.matdes.2012.05.003.
- [27] Y.W. Zhou, Y.F. Wu, Y. Yun, Analytical modeling of the bond-slip relationship at FRP-concrete interfaces for adhesively-bonded joints, Compos. B Eng. 41 (6) (2010) 423–433, https://doi.org/10.1016/j.compositesb.2010.06.004.
- [28] E. Radi, L. Lanzoni, A. Sorzia, Analytical modelling of the pullout behavior of synthetic fibres treated with nano-silica, Procedia Eng. 109 (2015) 525–532, https://doi.org/10.1016/j.proeng.2015.06.260.
- [29] T. D'Antino, P. Colombi, C. Carloni, L.H. Sneed, Estimation of a matrix-fiber interface cohesive material law in FRCM-concrete joints, Compos. Struct. 193 (2018) 103–112, https://doi.org/10.1016/j.compstruct.2018.03.005.
- [30] L.A. Le, G.D. Nguyen, H.H. Bui, A.H. Sheikh, A. Kotousov, Incorporation of micro-cracking and fibre bridging mechanisms in constitutive modelling of fibre reinforced concrete, J. Mech. Phys. Solids 133 (2019), 103732, https://doi.org/10.1016/j.jmps.2019.103732.
- [31] X. Zou, L.H. Sneed, T. D'Antino, C. Carloni, Analytical bond-slip model for fiber-reinforced cementitious matrix-concrete joints based on strain measurements, J. Mater. Civ. Eng. 31 (11) (2019) 04019247, https://doi.org/10.1061/(ASCE)MT.1943-5533.0002855.
- [32] S.K. Woo, Y. Lee, Experimental study on interfacial behavior of CFRP-bonded concrete, KSCE J. Civ. Eng. 14 (3) (2010) 385–393, https://doi.org/10.1007/s12205-010-0385-0
- [33] S. Mahjoubi, R. Barhemat, Y. Bao, Optimal placement of triaxial accelerometers using hypotrochoid spiral optimization algorithm for automated monitoring of high-rise buildings, Autom. Constr. 118 (2020), 103273, https://doi.org/10.1016/j.autcon.2020.103273.
- [34] A. Kaveh, S. Mahjoubi, Hypotrochoid spiral optimization approach for sizing and layout optimization of truss structures with multiple frequency constraints, Eng. Comput. 35 (4) (2019) 1443–1462, https://doi.org/10.1007/s00366-018-0675-6.
- [35] Y. Bao, Y. Chen, M.S. Hoehler, C.M. Smith, M. Bundy, G. Chen, Experimental analysis of steel beams subjected to fire enhanced by Brillouin scattering-based fiber optic sensor data, J. Struct. Eng. 143 (1) (2017) 04016143, https://doi.org/10.1061/(ASCE)ST.1943-541X.0001617.
- [36] L. Palmieri, L. Schenato, Distributed optical fiber sensing based on Rayleigh scattering, Open Opt. J. 7 (1) (2013) 104–127, https://doi.org/10.2174/1874328501307010104.
- [37] Z. Ding, C. Wang, K. Liu, J. Jiang, D. Yang, G. Pan, Z. Pu, T. Liu, Distributed optical fiber sensors based on optical frequency domain reflectometry: A review, Sensors 18 (4) (2018) 1072, https://doi.org/10.3390/s18041072.
- [38] "LUNA ODISI 6000 data sheet." https://lunainc.com/sites/default/files/assets/files/data-sheet/LUNA%200DiSI%206000%20Data%20Sheet.pdf. Accessed on January 1, 2023.